Physics at Future Linear e^+e^- Colliders

Keisuke Fujii
KEK, Tsukuba 305, Japan

Abstract

Physcis at future linear e^+e^- colliders are discussed from an experimental point of view with emphasis put on the energy range 300 to 500 GeV.

Talk presented at 22-nd INS International Symposium on
Physics with High Energy Colliders
March 8-10, Hongo, Tokyo

Physics at Future Linear e^+e^- Colliders

Keisuke Fujii: KEK, Tsukuba 305, Japan

Abstract

Physcis at future linear e^+e^- colliders are discussed from an experimental point of view with emphasis put on the energy range 300 to 500 GeV.

1 Introduction

The best map we have at present for future linear e^+e^- collider physics is the standard model which consists of three sectors: the gauge sector ($\mathcal{L}_{gauge}$), the Higgs sector ($\mathcal{L}_{Higgs}$), and the Yukawa sector ($\mathcal{L}_{Yukawa}$). Its remarkable phenomenological success is, however, essentially confined to the gauge sector: the matter-fermion-gauge-boson couplings in particular. Precision tests of gauge-boson self-couplings are still necessary to fully establish the gauge nature of the W and Z bosons. The remaining two sectors ($\mathcal{L}_{Higgs}$ and $\mathcal{L}_{Yukawa}$) are almost totally unknown, reflecting the fact that there are two missing particles, top and Higgs, yet to be discovered. The primary goal of next generation linear e^+e^- colliders is to look for these two missing particles and to explore the two unknown sectors through their studies. Precision tests of the unknown parts will lead us to new physics beyond the standard model for which supersymmetry (SUSY) is one of the most attractive possibilities. Our main targets thus include W/Z, top, Higgs, and SUSY.

Now the question is, what energy should we go to study them? We all know that the top quark must exit, since the bottom quark has been confirmed to belong to an isospin doublet[1]. Moreover, we have reasonably good, although indirect, estimates of the top quark mass from global fits to precision electroweak data: $m_t = 177 \pm 14$ GeV for $m_H = 300$ GeV[1], for instance. The energy range $\sqrt{s} = 300$-500 GeV thus covers the $t\bar{t}$ threshold and guarantees opportunities to study top quark pair productions.

Although there are no such solid mass bounds for the Higgs boson, we have a very interesting clue. Fig.1 shows the history of $\sin^2\theta_W$ measurements. We can see that the precision of the measrements improved dramatically after SLC and LEP and the measured $\sin^2\theta_W$ now converges to a value consistent with the minimal SUSY-$SU(5)$ model. The SUSY-$SU(5)$ model requires a Higgs boson lighter than 180 GeV[2]. The existence of a Higgs boson with $m_H \lesssim 200$ GeV[3] is a general consequence of GUT or Grand Desert hypothesis, since it implies that the four-point self-coupling of the Higgs boson should stay perturbative up through the Grand Desert to a very high energy scale. As we will see later, such a light Higgs boson can readily be discovered at a linear e^+e^- collider covering the same energy range $\sqrt{s} = 300$-500 GeV as required by top quark studies. If this is indeed the case, we may also expect to observe a lot of SUSY particles below 1 TeV. If not, the Higgs sector is, most probably, strongly interacting and its full understanding will have to await the exploration of multi-TeV region. It should, therefore, be emphasized that the light Higgs search will be a crucial branch point to decide the future direction of high energy collider physics.

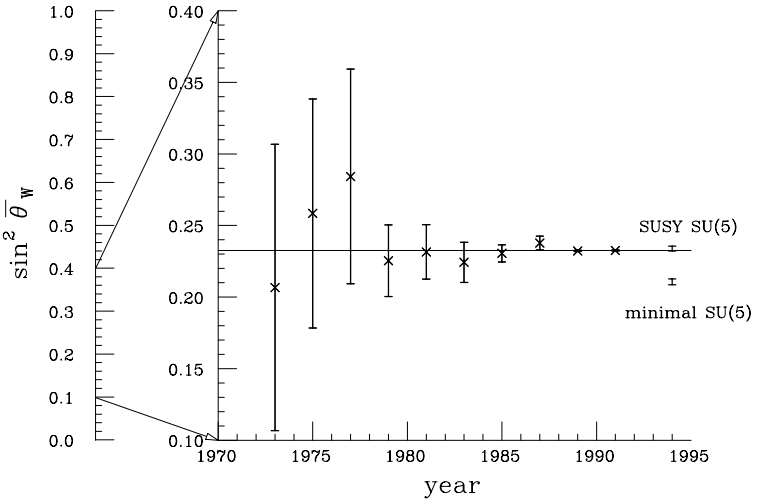

Figure 1: The history of the measurements of the Weinberg angle, compared with the predictions of the minimal (non-SUSY) $SU(5)$-GUT and the minimal SUSY $SU(5)$-GUT.

Now that the target energy region is fixed, the next question is the required luminosity. Fig.2 plots cross sections for various processes of interest as functions of $\sqrt{s}$. Inspection of the figure tells us that a luminosity of $L = 5 \times 10^{32}$ cm^{-2}sec^{-1} will be necessary for discoveries, while a luminosity in excess of $L = 5 \times 10^{33}$ cm^{-2}sec^{-1} will be desirable for precision studies.

2 Accelerator R&D

In the previous section, we have set the energy and the luminosity goals for next generation linear e^+e^- colliders from physics point of view. In this section, let us very quickly review the present status of accelerator R&D's and the prospects for construction of such a collider.

Our target energy, $\sqrt{s} = 500$ GeV, requires two main linacs each with $E_{beam} = 250$ GeV. In order to achieve this beam energy within limited length, say, 10 km, the acceleration gradient of each linac must exceed 25 MeV/m. This necessitates a high power RF system which includes a high power klystron, a pulse compression system, and a high gradient accelerating structure. R&D's on the high power RF system are in progress as worldwide efforts and are producing many remarkable results.[4]. For instance, an acceleration gradient of 40 MeV/m has already been achieved at KEK with a 100 MW S-band klystron and a new improved SLED cavity[5]. We can, thus, say that a power source is available.

The luminosity (L) of a collider is given by

$$L = \frac{N^2 f}{4\pi\sigma_x^*\sigma_y^*} H(D), \tag{2.1}$$

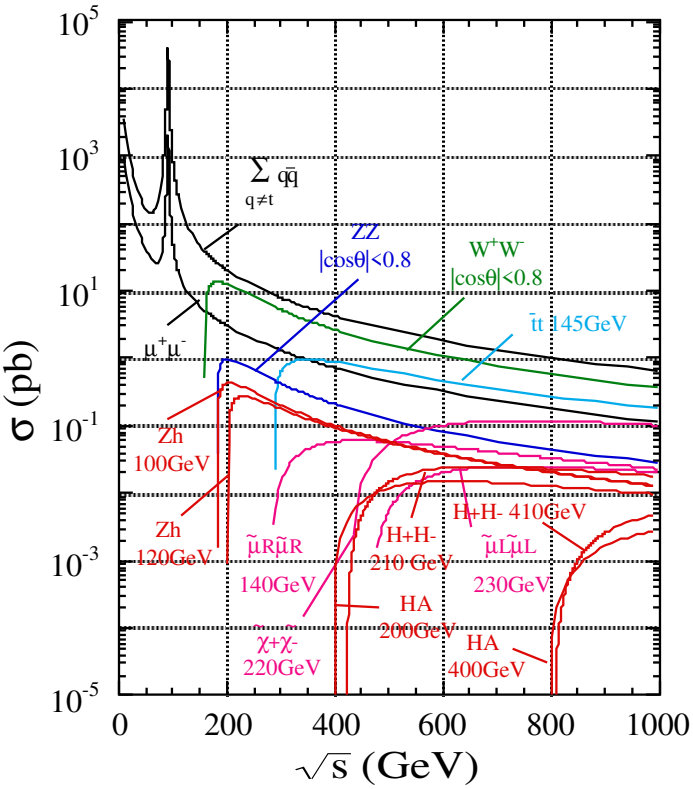

Figure 2: Cross sections for various processes of interest at future linear e^+e^- colliders.

where N is the number of particles per bunch, f the number of bunches per train times the repitition rate, σ_x^* and σ_y^* representing the beam spot size at the interaction point, and $H(D)$ the pinch enhancement factor. In practice, the available electric power (P) is limited and is related to beam parameters:

$$P = N \cdot f \cdot E/\eta, \tag{2.2}$$

where E is the beam energy and η is the acceleration efficiency. At the same time, we need to restrict the beam-beam force to keep the background due to beam-beam interactions under control. The beam-beam force is proportional to

$$\kappa = \frac{N}{\sigma_x^* + \sigma_y^*} \tag{2.3}$$

Substituting eqs.2.2 and 2.3 in eq.2.1, we obtain

$$L = \frac{P\eta\kappa}{4\pi}\left(\frac{1}{\sigma_x^*} + \frac{1}{\sigma_y^*}\right) H(D). \tag{2.4}$$

Since we cannot change P and κ and since $H(D)$ is of $O(1)$ in practice, the only way to increase L is to make the beam spot size small. It should also be noted that a flat beam is preferred to a round beam.

Our luminosity goal, $L \simeq 5 \times 10^{33}\mathrm{cm}^{-2}\mathrm{sec}^{-1}$, corresponds, for instance, to $\sigma_x^* \simeq$ 300 nm and $\sigma_y^* \simeq 3$ nm, when $N = 10^{10}$ and $f = 100 \times 50$. Such a tiny spot size requires (1) ultra low emittance beam and (2) nanometer beam handling technique. The Accelerator Test Facility (ATF) at KEK now under construction aims at achieving an invariant emittance of $\gamma\epsilon_y \simeq 3 \times 10^{-8}$ radm and will be completed in three years[6]. On the other hand, the Final Focus Test Beam (FFTB)[7] at SLAC is now ready to focus the 50 GeV SLAC beam to $\sigma_y^* \simeq 60$ nm which is limited mainly by the beam emittance available with the present damping ring at SLAC. We expect first results on the beam focusing and the spot size measurement this spring and, if successful, they will make a proof of principle for the nanometer beam handling.

We now think that almost all the technological problems have been solved in principle and, in three years, we will finish system tests and be ready for construction of a 500 GeV linear e^+e^- collider.

3 Detector

In order to make full use of the potential of the future linear collider we discussed in the previous section, we need to build a good detector. The detector should take into account new features of the future linear collider experiments.

Firstly, since jets become jettier and calorimetric resolutions get better with energy, we will be able to identify heavy partons such as W/Z bosons and t-quarks by reconstructing their hadronic decays with jet-invariant-mass method. Full reconstruction of final states in this way is possible only in the clean environment of an e^+e^- collider and will allow us to measure the four-momenta of final-state partons, where partons include light quarks, charm, bottom, and top quarks, charged leptons, neutrinos as missing four-momenta, photons, W, Z, and gluons. For the heavy partons which involve decays, we may even be able to measure their spin polarizations. This is perhaps the most important new feature which makes unique the future linear collider experiments: the Feynman diagrams behind a reaction become almost directly observable. The detector must take advantage of this and, therefore, has to be equipped with high resolution tracking and calorimetry for the jet-invariant-mass method, high resolution vertexing for heavy-flavor tagging, and hermeticity for indirect neutrino detection as missing momenta.

There is, however, a potentially serious problem inherent in linear collider experiments which is new kinds of background induced by beam-beam interactions. The beam-beam background includes low energy e^+e^- pairs and so called mini-jets. We cannot cover this topic today, but it has been shown that we can survive these with a carefully designed background mask system and detectors with good time resolution[8].

Fig.3 is a JLC example of possible detectors which satisfy the above requirements, where both the central tracking chamber (CDC) and the calorimeter (CAL) are put in a solenoidal magnetic field of 2 Tesla to achieve good resolution and hermeticity. Notice

that final focus quadrupole magnets and a background mask system are supported by a support cylinder which is installed in the detector and they should, thus, be considered as part of the detector system. The parameters and the design performance of the JLC

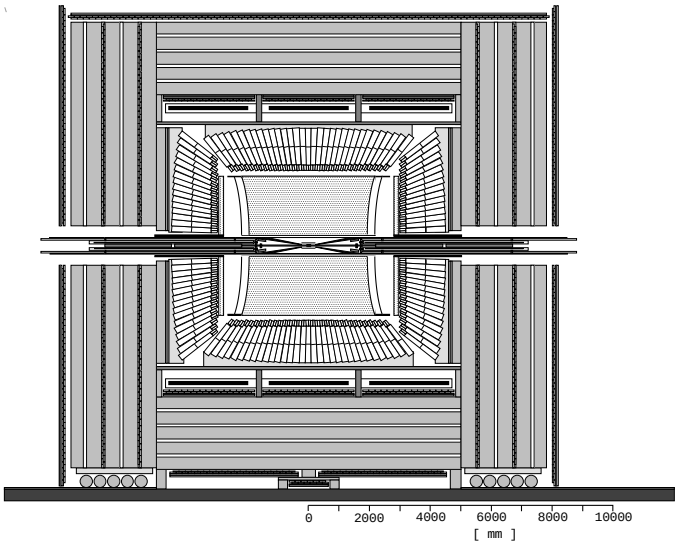

Figure 3: Schematic view of the JLC detector.

detector are summarized in Table 1.

DETECTOR	TYPE	CONFIGURATION	PERFORMANCE
VTX (Vertex Detector)	Silicon CCD	Pixel Size ; 25 μm Number of Layers ; 2 layers Layer Position ; r=2.5cm & 7.5cm Thickness ; 500 μm / layer $\|\cos\theta\| < 0.95$	Position Resolution ; σ = 7.2 μm Impact Parameter Resolution δ [μm]; $\delta^2 = 11.4^2 + (28.8/p)^2 / \sin^3\theta$
CDC (Central Drift Chamber)	Small-cell Jet Chamber	Radius ; r = 0.3 - 2.3 m Length ; l = 4.6 m Number of Sampling = 100 $\|\cos\theta\| < 0.70$ (full sampling) $\|\cos\theta\| < 0.95$ (20 samplings)	Position Resolution ; σ_x = 100 μm (/ axial wire) σ_z = 2 mm (/ stereo wire) Momentum Resolution ; σ_{Pt} / Pt = 1.1x10^{-4} Pt $\oplus$ 0.1% σ_{Pt} / Pt = 5 x10^{-5} Pt $\oplus$ 0.1% (with vertex constraint)
CAL	Lead + Plastic Scintillator Sandwitch (Compensated)	EM part ; thickness = 29 Xo cell size = 10cm x 10cm HAD part ; thickness = 5.6 λo cell size = 20cm x 20cm Si Pad ; pad size = 1cm x 1cm $\|\cos\theta\| < 0.99$	Energy Resolution ; $\sigma_E/\sqrt{E}$ = 15% / $\sqrt{E}$ $\oplus$ 1% (e & γ) $\sigma_E/\sqrt{E}$ = 40% / $\sqrt{E}$ $\oplus$ 2% (hadron) Si Pad Position Resolution ; σ = 3 mm Si Pad e/π Rejection = 1/50
MUON	Single Cell Drift Chamber	Number of Superlayers ; 6 $\|\cos\theta\| < 0.99$	Position Resolution ; σ = 500 μm Pt > 3.5 GeV (barrel)

* All momentum and energy are expressed in [GeV].

Table 1: Parameters and performance of the JLC detector

4 Examples of Simulated Experiments

Now that we have the machine and the detector defined, we can carry out Monte Carlo simulations to study feasibility of various physics. We begin with the top quark and then move on to the Higgs boson which is followed by SUSY. The case in which no light Higgs is found is treated briefly at the end of this section.

4.a Top

We now know that the top quark is heavier than the W boson and is lighter than 200 GeV, which implies the following. (i) The top quark is certainly in the next linear collider's reach. (ii) There is a chance to see the top Yukawa interaction. (iii) The decay into bW essentially saturates the branching fraction in the standard model and is dominant in most of its extensions. Because of this, the identification of the top quark should be no problem. (iv) The top quark has a large width which grows as m_t^3, once the bW mode is open: for instance, the width is about 1 GeV for $m_t = 150$ GeV which becomes as large as 2.5 GeV for $m_t = 200$ GeV. It is this large width that makes the top quark distinct from the lighter quarks. In fact, the large width acts as an infrared cutoff: the t or $\bar{t}$ created at $r = 0$ decays before entering the non-perturbative QCD regime of the $t\bar{t}$ potential, which allows us to calculate the production cross section with perturbative QCD[9]. We can, therefore, carry out clean tests of perturbative QCD and precision measurements of the QCD coupling α_s. Moreover, since the QCD effects are now under control, we will be able to extract other smaller effects such as the contribution from the Higgs exchange between the t and $\bar{t}$ quarks.

4.a.1 Threshold Scan

We begin with the total cross section measurments for $t\bar{t}$ pair production in the threshold region (threshold scan). The total cross section depends on the following parameters:

$$\sigma_{t\bar{t}}(\sqrt{s}; m_t, \Gamma_t, \alpha_s(m_Z), m_H, \beta_H),$$

where m_t is the top mass, Γ_t the top width, m_H the Higgs mass, and β_H the top Yukawa coupling normalized by its standard model value. Our goal is to determine these parameters by the threshold scan.

The signature of $t\bar{t}$ pair production is two b quarks and two W bosons in the final state, which, depending on the W's decay modes, results in the following three configurations: six jets (45%), or one lepton plus four jets (44%), or two leptons plus two jets (11%). Selection criteria for these final states have been studied by several authors[10] and we will skip their details. Instead, we just note that basic cuts include those on event shape variables such as the number of particles, the number of jets, and the thrust, those on jet invariant masses to identify W's and t's, and cuts to select an energetic isolated lepton if necessary. The b tagging with a vertex detector is very powerful, though we can do without it. Anyway, we can easily achieve a signal-to-background ratio greater than 10

with a reasonable overall detection efficiency around 30%, in spite of the huge background from W^+W^- pair productions.

The selected sample of $t\bar{t}$ events can be used to determine various parameters that enter the cross section formula[10]. Fig.4-a) is an example of threshold scan. The points with error bars in the figure are the Monte Carlo data generated with $m_t = 150$ GeV, $|V_{tb}|^2 = 1$, $\alpha_s(m_Z) = 0.12$, and $m_H = \infty$ (no Higgs). Each Monte Carlo data point corresponds to 1 fb^{-1} which is equivalent to 2 days of running at our luminosity goal: $L = 5\times10^{33}$ cm^{-2}sec^{-1}. The three curves in the same figure are the theoretical predictions for three values of $\alpha_s(m_Z)$, where the effects of initial state radiation and beamstrahlung are convoluted. We can see that, as $\alpha_s(m_Z)$ increases, the $t\bar{t}$ potential gets deeper and the position of the shoulder, which is the remnant of the $1S$ resonance, shifts downward. At the same time, the cross section increases since the absolute value of the wave function at the origin gets larger. A two-parameter fit to the Monte Carlo data results in the contour plot in Fig.4-b). The strong correlation between m_t and $\alpha_s(m_Z)$ stems from the fact that the downward shift of the $1S$ position by increasing $\alpha_s(m_Z)$ can be compensated by the upward shift by increasing m_t. Nevertheless, we can determine the top mass to a statistical accuracy of $\Delta m_t \simeq 0.2$ GeV, even if $\alpha_s(m_Z)$ is totally unconstrained. The corresponding statistical error on $\alpha_s(m_Z)$ is $\Delta\alpha_s(m_Z) \simeq 0.005$.

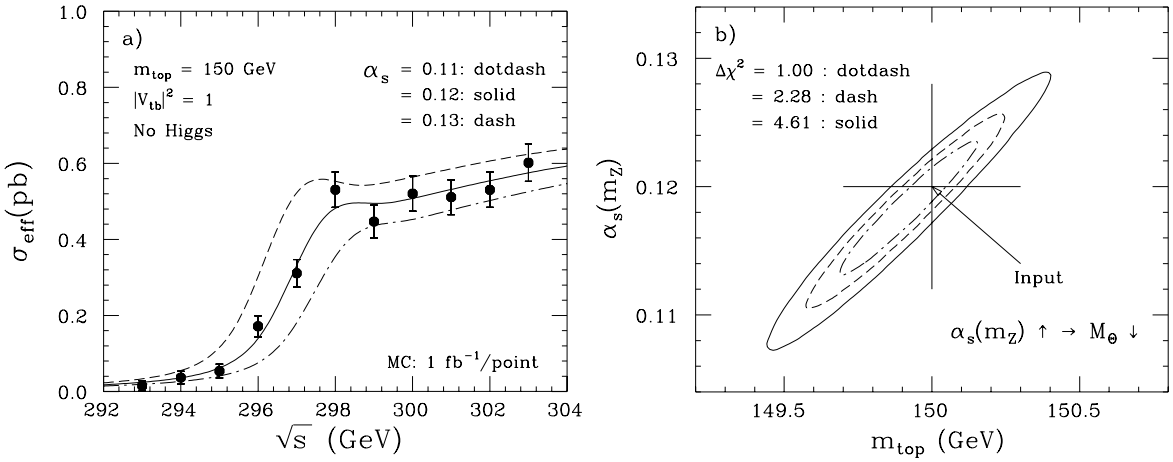

Figure 4: (a) An example of energy scan to determine m_t and $\alpha_s(m_Z)$ where each point corresponds to 1 fb^{-1}. (b) The contours resulting from the fit to the data points.

We can fit the same Monte Carlo data points with m_t and $|V_{tb}|^2$ as free parameters, where $|V_{tb}|^2$ is the top width normalized by its standard model value for $|V_{tb}|^2 = 1$. Notice that $|V_{tb}|^2$ in this definition can be larger than unity, if there is some non-standard model decay. Fig.5-a) compares the same Monte Carlo data points with theoretical predictions for three values of $|V_{tb}|^2$. We can see that, as the width gets narrower, the cross section at the $1S$ state increases, while that at the tail decreases. Notice that the $1S$ position is quite insensitive to the width change. This is why the correlation between m_t and $|V_{tb}|^2$ is very weak as demonstrated by the contours in Fig.5-b). The expected statistical error on the top width is $\Delta\Gamma_t/\Gamma_t \simeq 0.2$.

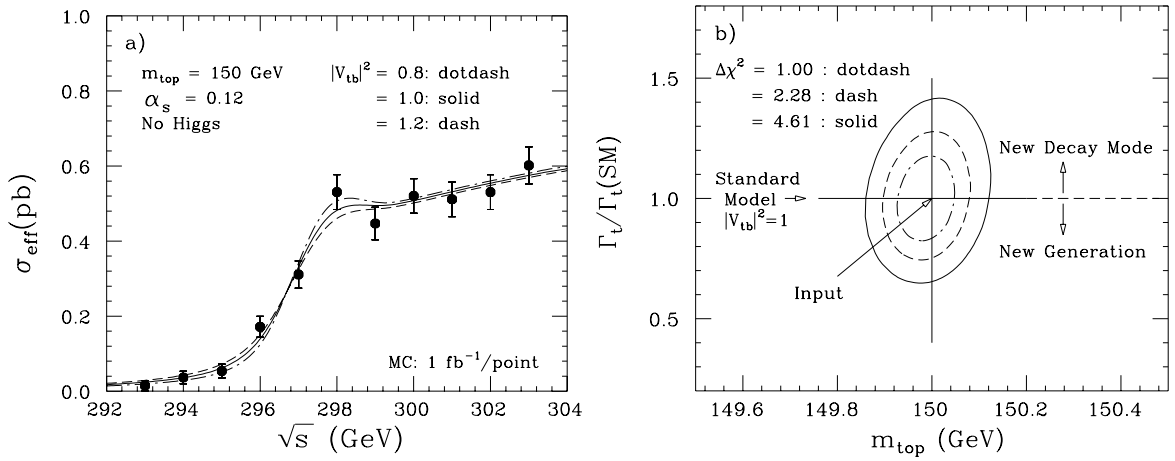

Figure 5: (a) An example of energy scan to determine m_t and $|V_{tb}|^2$ where each point corresponds to 1 fb^{-1}. (b) The contours resulting from the fit to the data points.

More interesting is the measurement of the top Yukawa coupling, using the threshold scan data. The effect of the Higgs exchange between t and $\bar{t}$ is approximately given by an attractive Yukawa potential:

$$V_H(r) = -\frac{\sqrt{2}G_F}{4\pi}(\beta_H m_H)^2 \frac{e^{-m_H r}}{r}.$$

Notice that, the Yukawa potential being of short range, the Higgs exchange affects only the overall normalization of the cross section. The dependence of the cross section on m_H and β_H^2 are shown, respectively, in Figs.6-a) and -b) together with the same Monte Carlo data points. The smaller the Higgs mass and the larger the Yukawa coupling, the larger the cross section becomes. Fig.6-c) is the contour plot resulting from a two-parameter fit to the Monte Carlo data. We can conclude that the expected statistical error on the Yukawa coupling is $\Delta\beta_H \simeq 0.25$ for the standard model Higgs with $m_H = 100$ GeV.

4.a.2 Measurement of Momentum Distribution

It has been pointed out that the measurement of the top quark momentum distribution provides information independent of what is extractable from the total cross section[11]. The key observations are the following. (1) The onia of the lighter quarks decay via annihilations and the information on the constituent quark momentum is lost. On the other hand, the momentum of the top quark in a toponium can be reconstructed as the momentum sum of the three-jet system from a $t \to bW$ decay. The momentum measurement of the quark in a quarkonium is, thus, possible only for $t\bar{t}$ resonances. (2) The total cross section is proportional to the imaginary part of the Green function at $r = 0$:

$$\sigma_{t\bar{t}} \propto -Im \sum_n \frac{|\Psi_n(0)|^2}{E - E_n + i\Gamma_n/2},$$

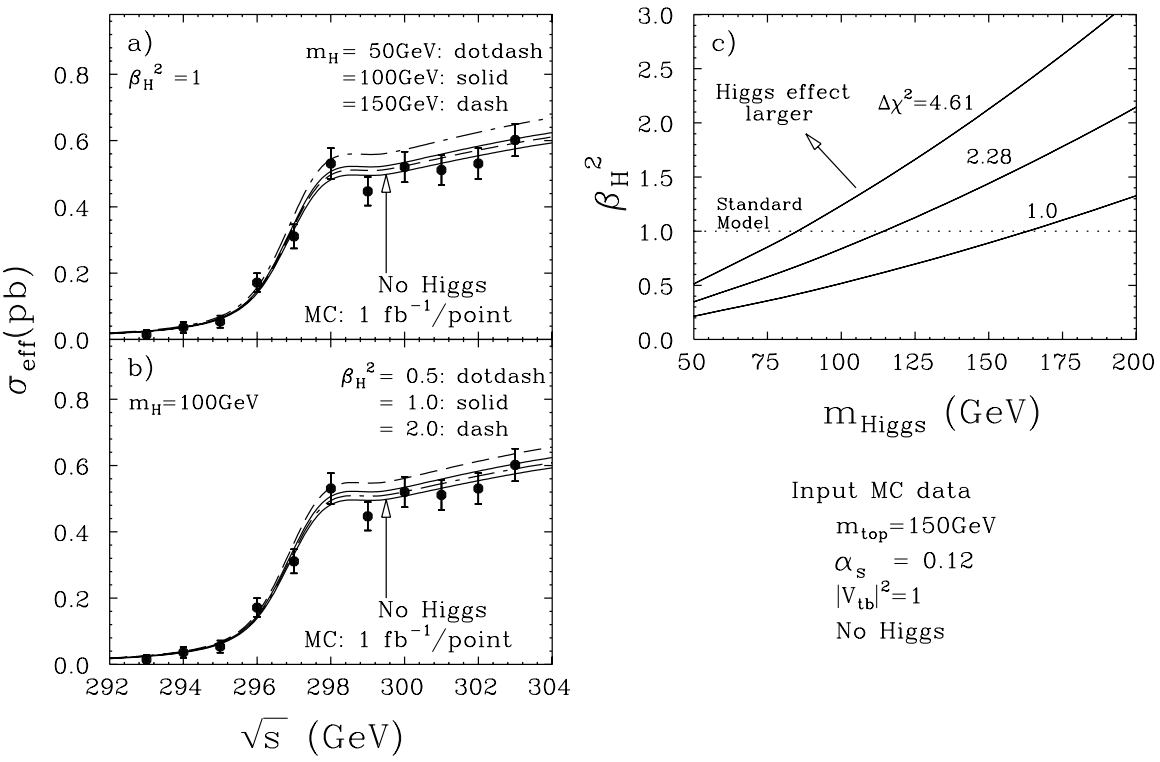

Figure 6: (a) An example of energy scan to determine m_H and β_H^2 where the effective cross section curves are superimposed for several m_H values. (b) The same plot with the effective cross section curves for several β_H^2 values. (c) The contours resulting from the fit to the data points.

which depends only on the wave function values at the origin, while the top momentum distribution carries the information on the momentum-space wave functions:

$$\frac{d\sigma_{t\bar{t}}}{d|\mathbf{p}_t|} \propto \left| \sum_n \frac{\phi_n(\mathbf{p}_t)\Psi_n^*(0)}{E - E_n + i\Gamma_n/2} \right|.$$

We can measure the momentum-space wave function which can be used as additional information for parameter determinations.

Now the question is, how well can we measure the top momentum distribution? To measure the top momentum distribution, we need at least one t or $\bar{t}$ quark which decays into three jets. The usable final state configurations are, thus, either a lepton plus four jets or six jets. The selection criteria for the momentum measurement must naturally be tighter than those used for the threshold scan, since we need to select well measured top quarks. We will not discuss the details of the selection here (see, for instance, Ref.[12] for details) but just show the results.

Fig.7-a) shows the reconstructed top momentum distribution (round points) compared with the scaled generated distribution (histogram) for the lepton+4-jet mode, where the Monte Carlo data were generated at the center-of-mass energy 2 GeV above the $1S$ peak with $m_t = 150$ GeV, $|V_{tb}|^2 = 1$, and $\alpha_s(m_Z) = 0.12$. The square points in the

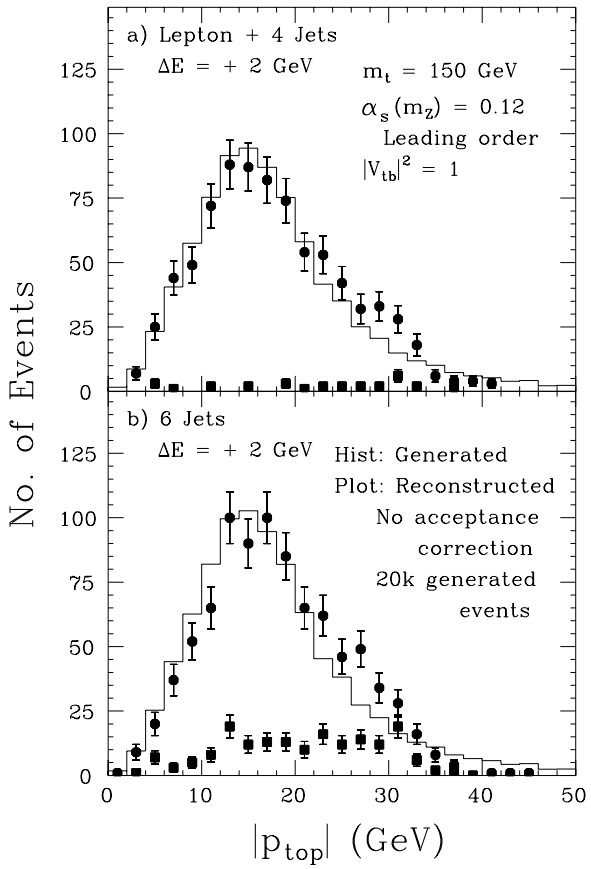

Figure 7: The reconstructed momentum distribution (round points) for (a) the lepton+4-jet mode and (b) the 6-jet mode, compared with the scaled generated distribution. The square points indicate the combinatorial background due to wrong jet assignment.

same figure represent the combinatorial background due to wrong jet assignment. We can see that the reconstructed momentum distribution reproduces the generated one well. On the other hand, the 6-jet mode suffers from the combinatorial background, since there are more jets in the final states. Although this combinatorial background can be reduced significantly, if we can eliminate charm quark contamination in the b-jet candidates from top decays, we conservatively assume, in what follows, that only the lepton+4-jet mode is usable. Then the expected statistical error on the momentum peak position is $\Delta|\mathbf{p}|_{peak} \simeq 0.13$ GeV for an integrated luminosity of 100 fb^{-1}.

Fig.8-a) shows the top momentum distributions at 2 GeV above the $1S$ peak for different $\alpha_s(m_Z)$ values, including initial state radiation and beam effects. We can see that the momentum peak shifts downward as $\alpha_s(m_Z)$ increases. The momentum peak position is given in Fig.8-b) as a function of $\alpha_s(m_Z)$. The error on the momentum peak position corresponds to $\Delta\alpha_s(m_Z) \simeq 0.002$, if the $1S$ peak position and the top width are known.

The momentum peak position also depends on the top width: the top decays where the potential is deeper when the width becomes larger, thereby making the momentum

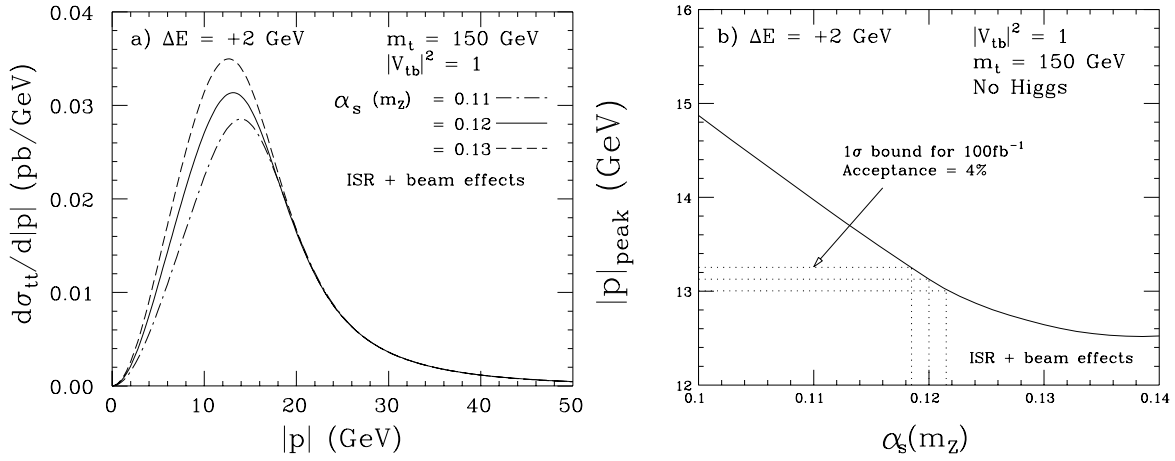

Figure 8: (a) The top momentum distribution at 2 GeV above the $1S$ peak, for $\alpha_s(m_Z) = 0.11, 0.12, 0.13$, and $m_t = 150$ GeV. (b) The momentum peak position as a function of $\alpha_s(m_Z)$. The dotted lines indicate the 1-σ bounds expected for an integrated luminosity of 100 fb^{-1}.

peak position higher (see Fig.9-a)). Fig.9-b) plots the momentum peak position as a function of the normalized top width $|V_{tb}|^2$. The expected statistical error on the top width is $\Delta\Gamma_t/\Gamma_t \simeq 0.04$ for the integrated luminosity of 100 fb^{-1}, if the $1S$ peak position and $\alpha_s(m_Z)$ are known.

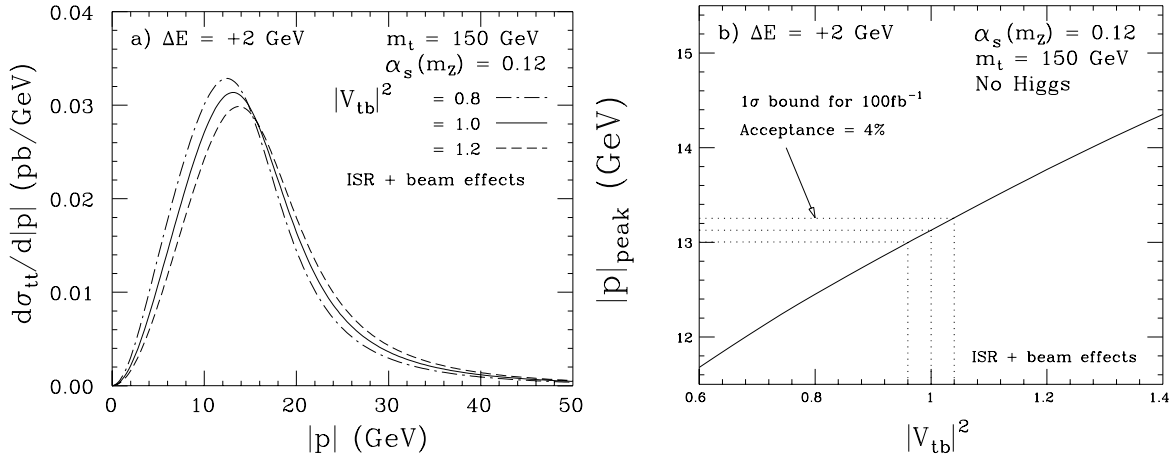

Figure 9: (a) Similar to Fig.8-a) but plotted for different top widths. (b) The momentum peak position as a function of $|V_{tb}|^2$. The dotted lines indicate the 1-σ bounds expected for and integrated luminosity of 100 fb^{-1}.

4.b Higgs

As stated earlier, the existence of a Higgs boson with $m_H \lesssim 200$ GeV is a general consequence of theories which assume a Grand Desert. If there is no Higgs in this mass range, therefore, that means the death of low energy SUSY and GUT. This is one of the most important branch points to decide future direction of high energy physics. LEP-II covers the Higgs mass range only up to about 90 GeV, while the future linear e^+e^- collder defined previously covers the Higgs mass up to about 400 GeV and will answer which way to go for sure.

4.b.1 Higgs Search

The best channel to produce the light Higgs boson is $e^+e^- \to Z^0H^0$, where the Higgs boson decays mainly into $b\bar{b}$. Depending on the three decay modes of the Z^0 boson (i) $Z^0 \to \nu\bar{\nu}$, (ii) $Z^0 \to l^+l^-$, and (iii) $Z^0 \to q\bar{q}$, we have the three independent search modes shown in Fig.10. The main bacground comes from the processes $e^+e^- \to Z^0Z^0$, $e^{\pm}\overset{(-)}{\nu_e}W^{\mp}$, and W^+W^-, which are effectively suppressed by selecting events produced in the central region with two b jets[13].

The Higgs will appear as a peak in the invariant mass distribution of the two-jet system, when we require the rest of the final state (two jets, two leptons, or nothing, depending on the topologies) be consistent with Z^0. Figs.11-a) to -c) are examples of the Higgs mass distributions reconstructed in the three search modes at the stage of $\int Ldt$=4fb^{-1} which is 8 days equivalent given the design luminosity of $L = 5 \times 10^{33}$ cm^{-2}sec^{-1}. In the figure, the hatched mass peaks correspond to m_H= 80, 100, 120, and 140 GeV, while the open histogram shows the background process: $e^+e^- \to Z^0Z^0$. A clean peak can be observed in the $\nu\bar{\nu}b\bar{b}$ and $q\bar{q}b\bar{b}$ modes already at 4fb^{-1}, if m_H is less than 160 GeV. If m_H exceeds 160 GeV, the other decay mode such as $H^0 \to W^+W^-$ will be useful for the Higgs discovery at the stages of low integrated luminosity.

Accumulation of 30 fb^{-1} will make the signal doubtless in all of the three search modes (see Fig.12), as long as the difference between m_H and m_Z is greater than $\sim$10 GeV. In the 2-lepton+2-jet mode, we can also look at the recoil mass opposite to the charged lepton pair. Fig.13-a) plots the recoil mass distribution of the signal process with different Higgs masses (hatched histogram) and that of the background process (open histogram) for the 30 fb^{-1} Monte Carlo data. Notice that the widths of the mass peaks are dominated by the beam energy spread which can be improved by colliding lower energy positrons with higher energy electrons or vice versa so as to keep the center-of-mass energy constant. Fig.13-b) is the improved recoil mass distribution after the energy control down to $\Delta\sqrt{s}/\sqrt{s} = 0.2\%$. Notice that this search method is independent of the decay modes of the Higgs boson and is viable even if all the H^0 decay modes are invisible.

The recoil mass measurement will become an indispensable tool in particular when the Higgs mass is close to m_Z. Even in this case, we can detect the existence of something new as an excess of events around m_Z. To confirm that it is indeed a Higgs boson, we then optimize $\sqrt{s}$ and the beam energy spread (Precision Run) and look at the recoil mass distribution.

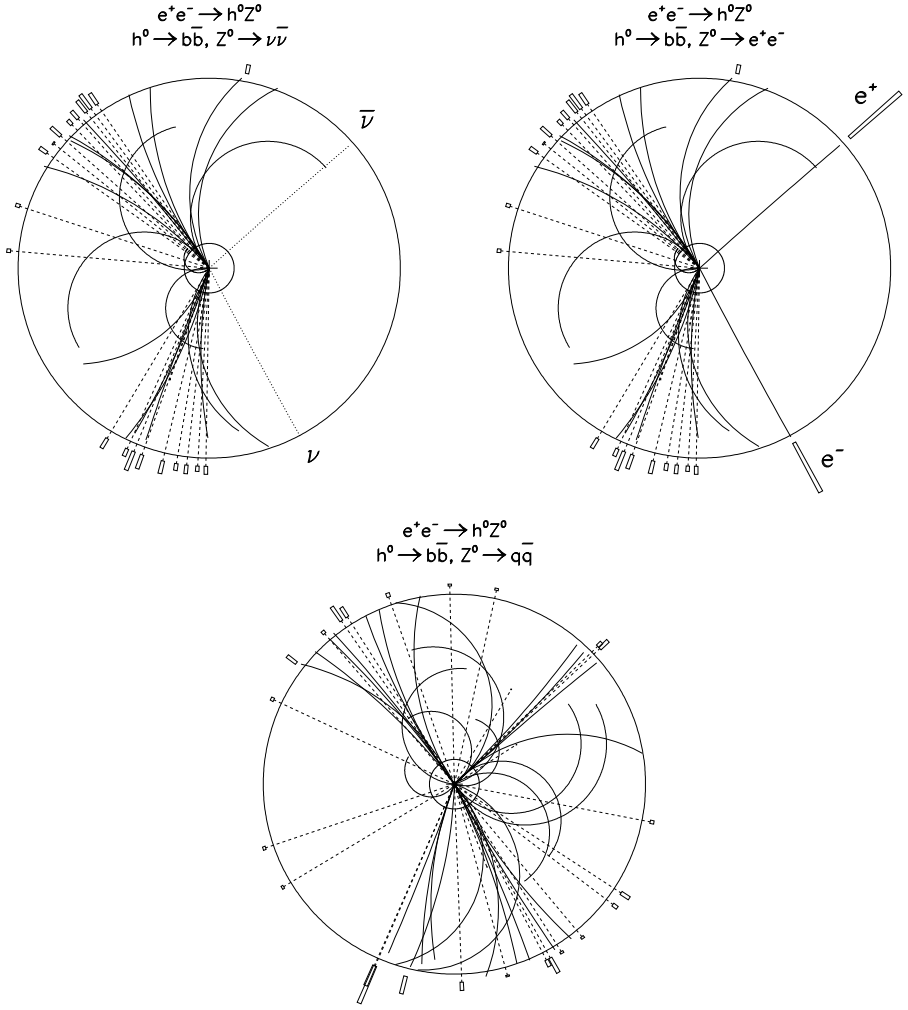

Figure 10: Typical $e^+e^- \to H^0Z^0$ events with $m_H = 120$ GeV at $\sqrt{s} = 300$ GeV: (a) $H^0 \to b\bar{b}$ and $Z^0 \to \nu\bar{\nu}$, (b) $H^0 \to b\bar{b}$ and $Z^0 \to l^+l^-$, and (c) $H^0 \to b\bar{b}$ and $Z^0 \to q\bar{q}$. In pictures (a) to (c), the solid curves represent tracks of the charged particles in the central tracking chamber with a magnetic field of 2.0 Tesla and active radius of 0.3 to 2.3 m, while the dotted lines show photon emissions. The surrounding boxes are electromagnetic clusters, and the lengths of the boxes correspond to their energies.

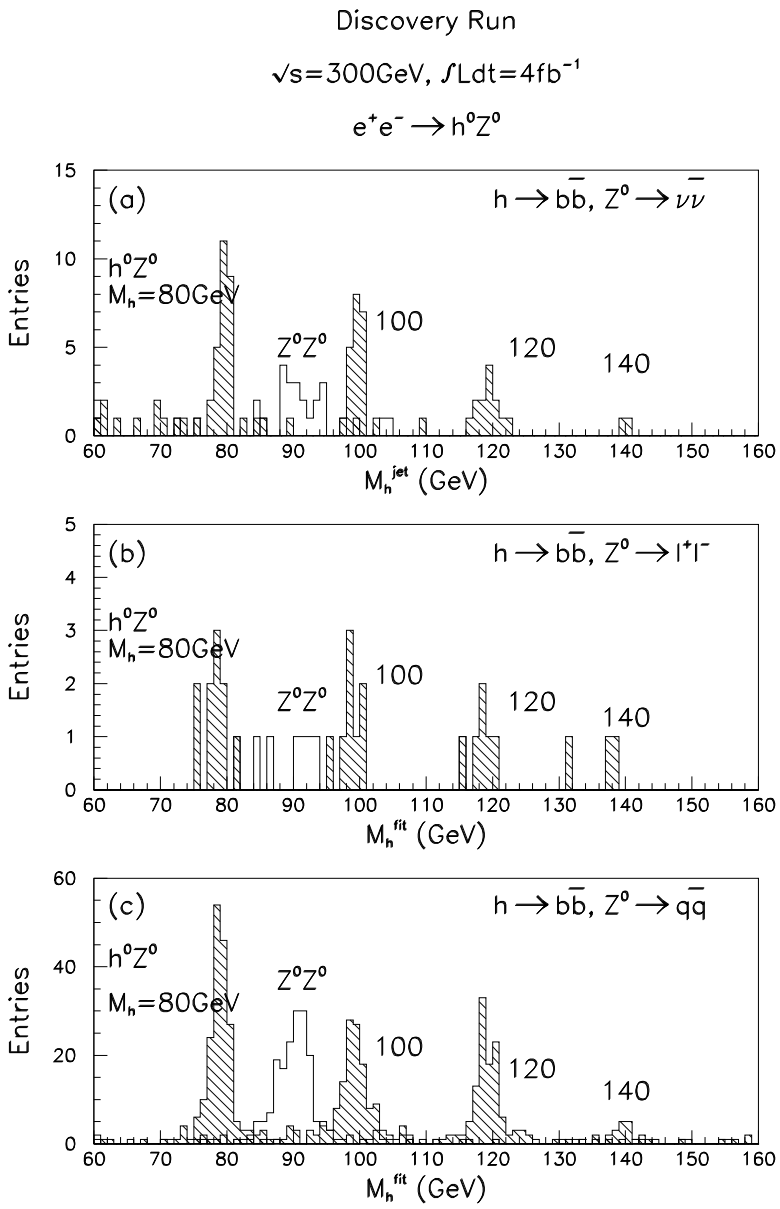

Figure 11: The reconstructed mass distributions for the three search modes after the Discovery Run of $\int Ldt = 4\text{fb}^{-1}$: (a) $H^0 \to b\bar{b}$ and $Z^0 \to \nu\bar{\nu}$, (b) $H^0 \to b\bar{b}$ and $Z^0 \to l^+l^-$, and (c) $H^0 \to b\bar{b}$ and $Z^0 \to q\bar{q}$. In the figures, the hatched histograms are for the signal process $e^+e^- \to H^0Z^0$ with m_H=80, 100, 120, and 140 GeV, while the open histograms are for the background process $e^+e^- \to Z^0Z^0$.

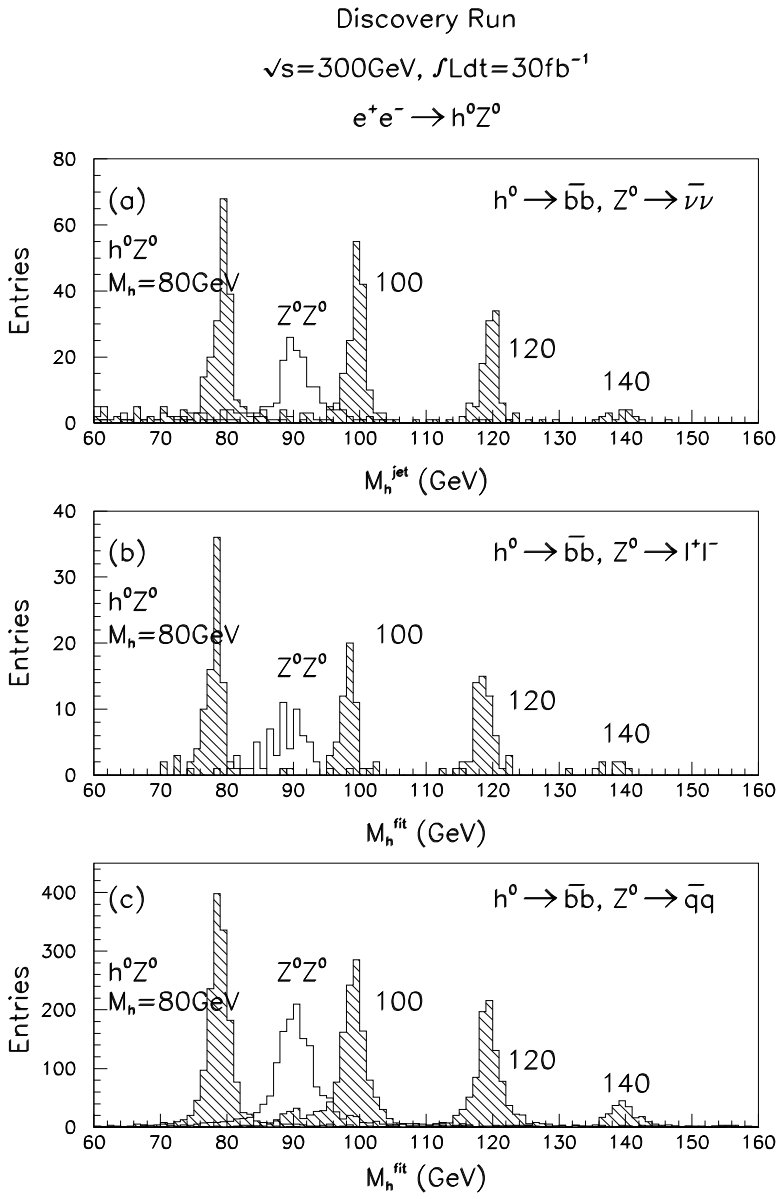

Figure 12: Same as Fig.11, but with an integrated luminosity of 30 fb^{-1}

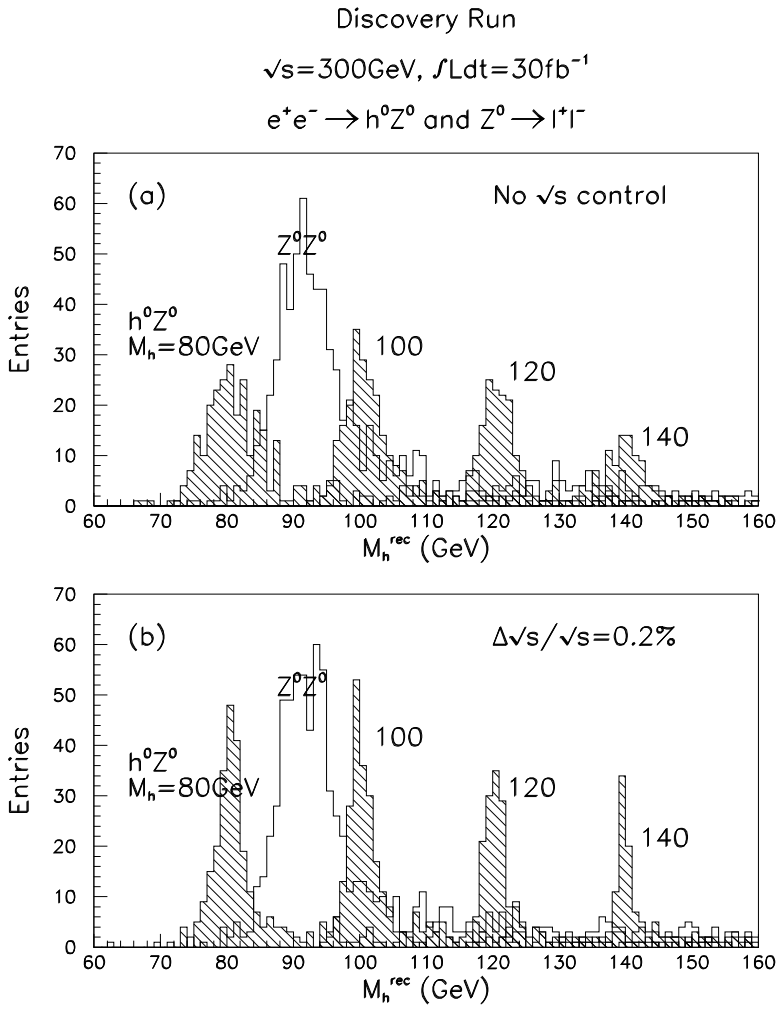

Figure 13: The distributions of the recoil mass opposite to the lepton pair in the 2-lepton+2-jet mode: (a) without and (b) with the $\sqrt{s}$ control, plotted without b-tagging. The hatched histograms are for the signal process $e^+e^- \to H^0Z^0$ with m_H=80, 100, 120, and 140 GeV, while the open histogram is for the background process $e^+e^- \to Z^0Z^0$.

Fig.14 shows the recoil mass distributions for $m_H = 85, 90, 95$, and 100 GeV together with the Z^0Z^0 background. The figure assumes an integrated luminosity of 10 fb^{-1} and the b-tagging of two b jets. We can see clear signal peaks sticking out from the Z^0Z^0 background. From the recoil mass distribution, we can measure the Higgs mass with a statistical error of $\Delta m_H \simeq$ 10-50 MeV and its width with $\Delta\Gamma_H \simeq 200$ MeV.

4.b.2 Precision Studies of Higgs Properties

Once a light Higgs particle is discovered, we set the center-of-mass energy at the maximum of the Higgs production cross section and carry out the Precision Run with the $\sqrt{s}$ control. The high statistics and high prcision data from the Precision Run will provide valuable information to answer the next crucial question, whether the discovered Higgs boson is that of the standard model or not. In the standard model, the Higgs width is of $O(5$ MeV), while it may become measurably large in its extensions such as the Minimal Supersymmetric Standard Model (MSSM). Fig.15 shows the contours of the total width of the MSSM Higgs in the m_A and $\tan\beta$ plane. When m_A is small and $\tan\beta$ is large, the total width of the MSSM Higgs becomes, indeed, very large due to the large Yukawa coupling to $b\bar{b}$. Since we can measure the total width down to 200 MeV, we can establish the non-minimality of the Higgs boson, when m_A is smaller than 120 GeV and $\tan\beta$ is greater than 8.

The total cross section of $e^+e^- \to h^0Z^0(\sigma_{Zh})$ multiplied by Br$(h \to b\bar{b})$ also provides information to judge if the discovered Higgs boson is that of the standard model or not. This quantity is proportional to the number of events observed in the $\nu\bar{\nu}h$ and $q\bar{q}h$ mode with b-tagging and can be measured with a statistical error of 2% (1-σ) for $m_h = 110$ GeV, when an integrated luminosity of 80 fb^{-1} is accumulated. The difference of the $\sigma_{Zh} \times Br(h \to b\bar{b})$ in the MSSM from the standard model($\Delta\sigma_{Zh}$) is shown in Fig.16 as contours in the m_A-$\tan\beta$ plane. In the small m_A region, $\Delta\sigma_{Zh}$ is negative because σ_{Zh} is smaller than the standard model value due to the $\sin(\beta - \alpha)$ factor in the ZZh vertex. In the large m_A region, however, σ_{Zh} rapidly converges to the standard model value. Nevertheless, $Br(h \to b\bar{b})$ is still significantly larger there than the standard model value, thereby extending the sensitivity to the large m_A region. These measurements will set strong constraints on the parameter space ($\tan\beta$,m_A) and will possibly establish the non-minimality of the discovered Higgs boson. The limits on m_A will be invaluable for the energy upgrade program of the next linear collider.

4.b.3 Other Higgses

In the presence of two Higgs doublets as in the case of the MSSM, we have extra Higgs particles: H^0, A, and $H^\pm$, in addition to the lightest one: h^0. If we are lucky, we might detect two or more Higgs particles. If this is the case, it will be the cleanest proof of the Higgs sector being non-minimal. Fig.17 is an example of this lucky situation, where we can see two mass peaks corresponding to h^0 and H^0 in the three search modes we discussed previously. We can also use the reactions $e^+e^- \to h^0/H^0 + A$ or $\to H^+H^-$ to search for the extra Higgs particles.

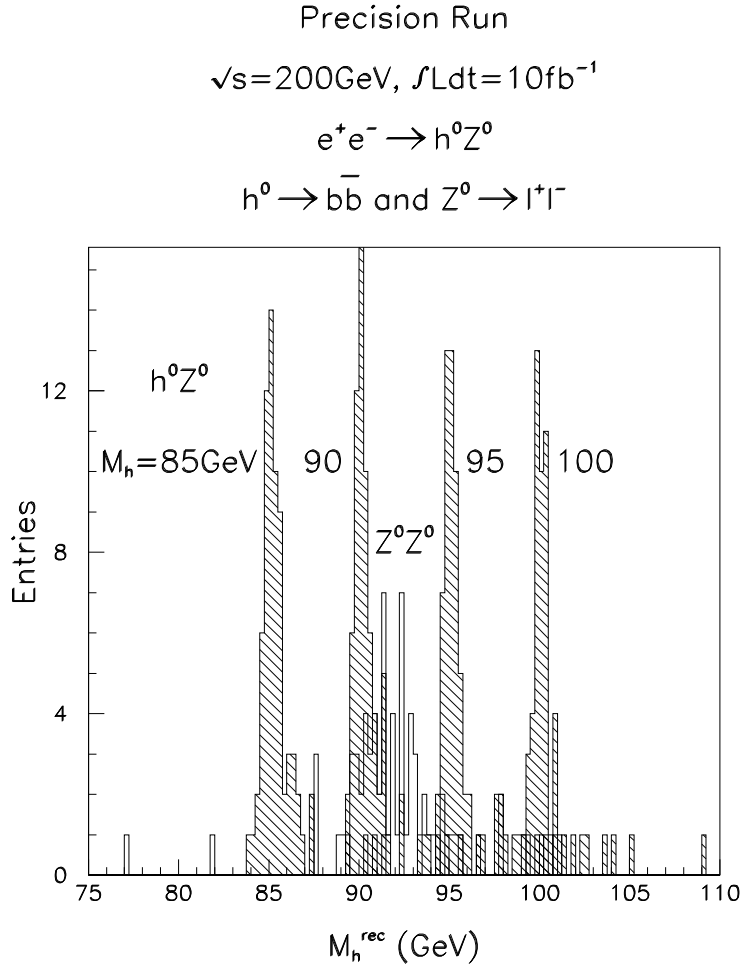

Figure 14: The distribution of the recoil mass opposite to the lepton pair in the decay channel: $H^0 \to b\bar{b}$ and $Z^0 \to l^+l^-$. The hatched histograms are for the signal process $e^+e^- \to H^0Z^0$ with m_H=85, 90, 95, and 100 GeV, while the open histogram is for the background process $e^+e^- \to Z^0Z^0$. The figure assumes an integrated luminosity of $\int Ldt = 10$ fb^{-1} with b-tagging.

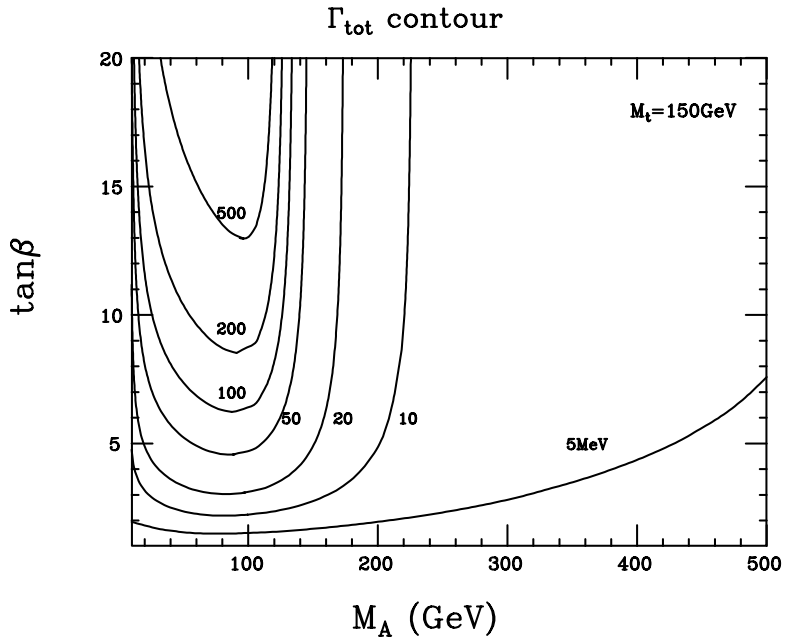

Figure 15: The contours of the total width of the MSSM Higgs h^0 in the m_A-tan β plane. In this calculation, we assumed $m_t = 150$ GeV and $m_{SUSY} = 1$ TeV, therefore, $m_h < 120$ GeV. The total width of the Standard Model Higgs (m_H) in this mass region is a few MeV at maximum.

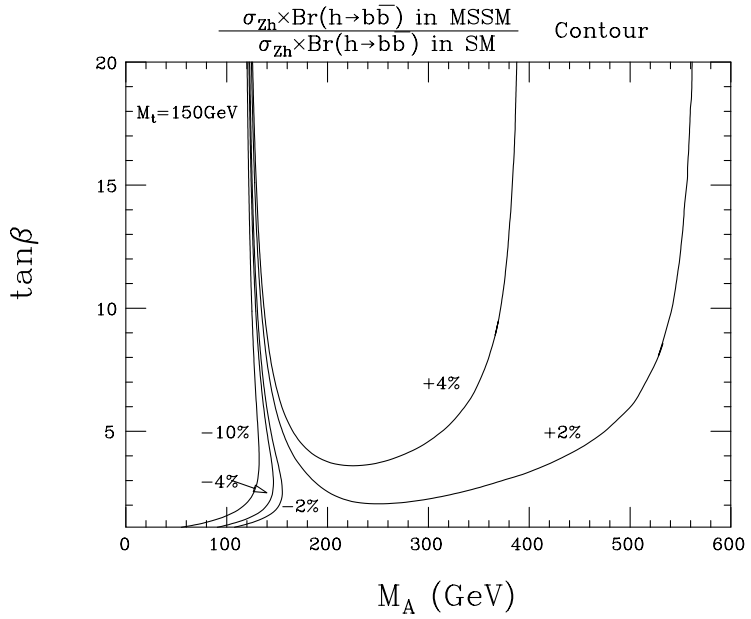

Figure 16: $\sigma \times Br(h^0 \to b\bar{b})$ in the MSSM compared with that of the Standard Model.

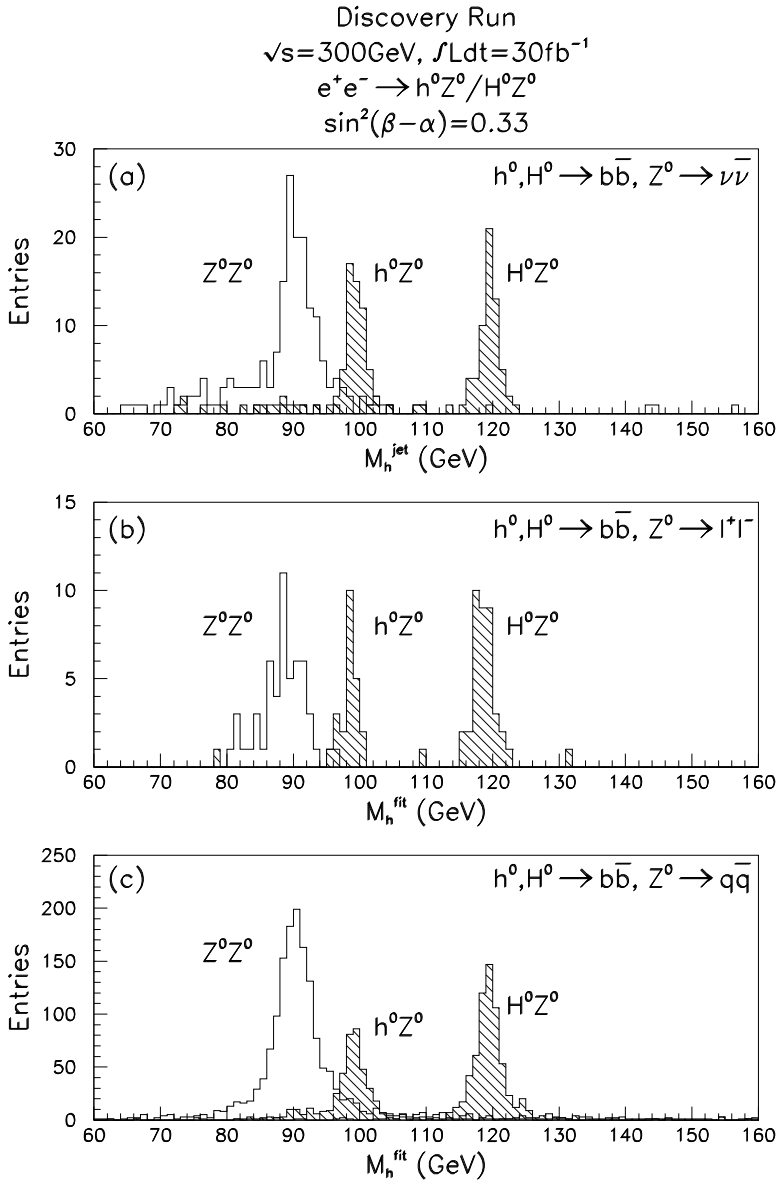

Figure 17: The reconstructed mass distributions for the three search modes after the Discovery Run of $\int Ldt$=30 fb^{-1}. In the figures, the hatched histograms are for the signal processes $e^+e^- \to h^0Z^0$ and $e^+e^- \to H^0Z^0$ with $m_h = 100$ GeV, $m_H = 120$ GeV, and $\sin^2(\beta-\alpha) = 0.33$, while the open histograms are for the background process $e^+e^- \to Z^0Z^0$. The b-tagging is assumed in the three modes.

4.c Supersymmetry

If there is a light Higgs boson, SUSY will become the most likely scenario. Nevertheless, the existence of the light Higgs boson alone is not enough to prove the low energy supersymmetry. It is absolutely necessary to find at least one SUSY particle. As we will see in what follows, the discovery of SUSY is relatively easy at a future linear e^+e^- collider. The discovery of a SUSY particle is, however, the beginning of the vast SUSY physics which might lead to the Planck world through the studies of the SUSY breaking sector. In this subsection, we will quickly go through the SUSY study scenario in the framework of the MSSM[14, 15].

In order to get insight into which SUSY particle is the first to be discovered, let us examine the mass relations of SUSY models. The grand unification of the gauge couplings implies the unification of gaugino masses at the GUT scale, leading to the following mass relation among the gaugino masses at the weak scale:

$$M_i = M \cdot \frac{\alpha_i(m_Z)}{\alpha_{GUT}} \qquad \text{with} \quad i = \begin{cases} 1 & : U(1)_Y \\ 2 & : SU(2)_L \\ 3 & : SU(3)_C \end{cases} .$$

The larger the group, the faster the running of the coupling. From this we have the following relation among the gaugino mass parameters: $M_1 : M_2 : M_3 \simeq 1 : 2 : 7$, which translates itself to an inequality:

$$m_{\tilde{\chi}_1^\pm} \lesssim \frac{1}{3} m_{\tilde{g}}.$$

The lighter chargino is, thus, expected to be significantly lighter than the gluino.

In the scalar fermion sector, we have mass formulae in the form:

$$m_{\tilde{f}}^2 = m_0^2 + G_{\tilde{f}} M_2^2 + D_{\tilde{f}} m_Z^2,$$

where the first term on the right-hand side is the square of the universal scalar mass, the second term represents the contribution from gauge interactions, and the last term stands for that of the D-term. Since the D-term is of $O(1)$ or less, the sfermion mass spectrum is essentially determined by the gauge term. The size of the gauge term is determined by the size of the gauge group relevant to the sfermion in question: $G_{\tilde{q}} > G_{\tilde{l}}$ since $3 > 2, 1$ and $G_{\tilde{f}_L} > G_{\tilde{f}_R}$ since $2 > 1$.

These mass relations suggest that the colorless SUSY particles are usually lighter than the colored ones and the right-handed sfermions are lighter than the left-handed ones:

$$\begin{aligned} m_{colorless} &< m_{colored} \\ m_{\tilde{f}_R} &< m_{\tilde{f}_L} \end{aligned}$$

Our first SUSY particle will, probably, be either the lighter chargino ($\tilde{\chi}_1^\pm$) or the right-handed sleptons ($\tilde{l}_R^\pm$). In the following, we take a sample case where the right-handed sleptons are the lightest charged SUSY particles and see how we can search and study SUSY. The SUSY parameters of our sample case are $(m_0, M_2, \mu, \tan\beta) = (70, 250, 400 \text{ GeV}, 2)$.

4.c.1 $\tilde{l}^{\pm}_R$ Search

The right-handed sleptons can be pair-produced in e^+e^- collisions via annihilations into a single γ or Z^0. To the pair production of right-handed selectrons, t-channel neutralino exchange diagrams also contribute, which can make the cross section significantly larger, when the Lightest SUSY Particle (LSP) is a neutralino dominated by bino component. In any case, the signal of the right-handed slepton pair production is an acoplanar lepton pair with large missing transverse momentum, since the right-handed sleptons, being the lightest charged SUSY particles, directly decay into the LSP.

The background to this signal process comes from the standard model processes with neutrinos which mimic the LSP. The key point is the power of polarized electron beam available at a future linear e^+e^- collider. For instance, the cross section of the largest standard model background, $e^+e^- \to W^+W^-$ followed by $W \to l\nu$ decays, essentially vanishes for a right-handed electron beam, since, in the symmetry limit, the W-pair in the s-channel only couples to W^0 and that in the t-channel involves a neutrino, both of which only couple to a left-handed electron: $\sigma_R(W^+W^-) \to 0$. On the other hand, the right-handed electron beam almost doubles the unpolarized cross section for the s-channel pair production of right-handed sleptons, since, in the symmetry limit, the particle exchanged in the s-channel becomes the $U(1)_Y$ gauge boson B whose coupling to a right-handed electron is twice larger than that to a left-handed electron: $\sigma_R(\tilde{l}^+_R\tilde{l}^-_R) \simeq 4\sigma_L(\tilde{l}^+_R\tilde{l}^-_R)$. Figs.18-a) and -b) are the acoplanarity angle distributions for the right-handed selectron and smuon pairs, respectively, when the electron beam polarization is zero and the integrated luminosity is 20 fb^{-1}. The solid histograms are the signal Monte Carlo data, while the

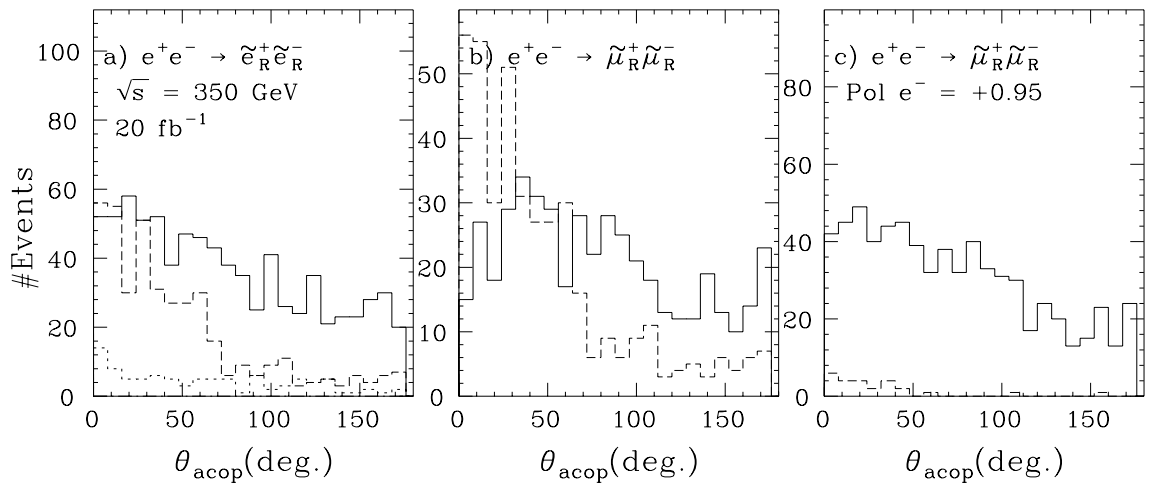

Figure 18: Acoplanarity angle distributions of final-state leptons from right-handed slepton pair productions (solid) at $\sqrt{s} = 350$ GeV with an integrated luminosity of 20 fb^{-1} after including the effects of initial state radiation and beamstrahlung: (a) $e^+e^- \to \tilde{e}^+_R\tilde{e}^-_R$ with $P_{e^-} = 0$, (b) $e^+e^- \to \tilde{\mu}^+_R\tilde{\mu}^-_R$ with $P_{e^-} = 0$, and (c) $e^+e^- \to \tilde{\mu}^+_R\tilde{\mu}^-_R$ with $P_{e^-} = +0.95$. The dashed lines indicate the W^+W^- background, while the dotted line represents that from the $e^{\pm}\overset{(-)}{\nu}_e W^{\mp}$ process.

dashed and the dotted ones are bacground from the W^+W^- and the $e^{\pm}\overset{(-)}{\nu}_e W^{\mp}$ processes, respectively. The backgrond processes are very effectively suppressed as in Fig.18-c), when the polarized electron beam is turned on to $P_{e^-} = +0.95$. With the help of an additional cut on the acoplanarity angle at, say, $\theta_A = 30°$, we can get a very clean sample of right-handed slepton pair productions.

The so selected sample of right-handed sleptons can be used to determine the masses of the sleptons and the LSP. For this purpose, we look at the energy distribution of the leptons from the slepton decays. Fig.19-a) is the muon energy distribution corresponding to Fig.18-c). The end points of the distribution carry the information on the smuon and the LSP masses, which can be extracted by a two-parameter fit to the Monte Carlo data. The smooth line in the same figure is the best-fit curve and those in Fig.19-b) are the contours in the $m_{\tilde{\mu}_R^{\pm}}$-$m_{\tilde{\chi}_1^0}$ plane. The figure demonstrates that 1% measurements are possible for both the smuon and the LSP masses.

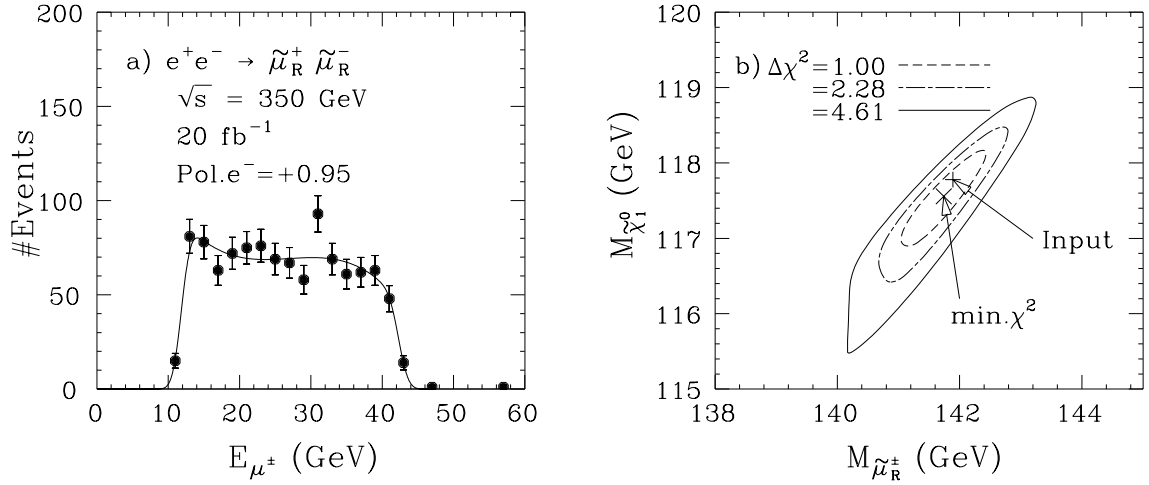

Figure 19: (a) The energy distribution of final-state muons corresponding to Fig.18-c). The smooth curve in the figure is the best-fit curve resulting from a two-parameter fit varying the $\tilde{\mu}_R^{\pm}$ and $\tilde{\chi}_1^0$ masses. (b) The corresponding χ^2 contours in the $m_{\tilde{\mu}_R^{\pm}}$-$m_{\tilde{\chi}_1^0}$ plane.

Even in this early stage of the SUSY studies, we can make a crucial test of one of our basic assumptions: the generation independence of the scalar masses which is a consequence of the hidden sector SUSY breaking or the universal scalar mass hypothesis. Fig.20 shows the expected 1-σ contour in the $m_{\tilde{e}_R^{\pm}}$-$m_{\tilde{\mu}_R^{\pm}}$ plane, compared with the prediction of the universal mass hypothesis indicated by a dotted line.

Once the masses of the sleptons and the LSP are known, we can solve the kinematics and reconstruct the production angle up to a two-fold ambiguity. Fig.21-a) plots, with the two-fold ambiguity unresolved, the distribution of the reconstructed production angles for the Monte Carlo $\tilde{\mu}_R$-pair data corresponding to Fig.18-c). The histogram in the same figure is the distribution of right solutions after selection cuts, comparison of which with the data points suggests that wrong solutions make a flat distribution. Such a flat background is easy to subtract and we obtain Fig.21-b), where the histogram shows the

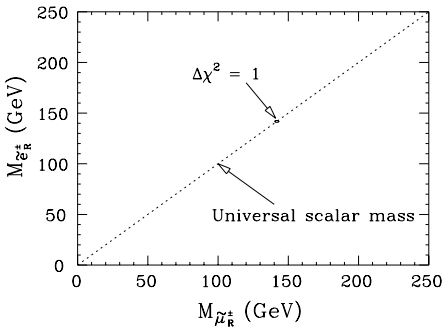

Figure 20: The $\Delta\chi^2 = 1$ contour in the $m_{\tilde{e}_R^\pm}$-$m_{\tilde{\mu}_R^\pm}$ plane obtained from the fits to the final-state lepton energy distributions for the $\tilde{\mu}_R$- and $\tilde{e}_R$-pair productions. The dotted line represents the universal scalar mass hypothesis.

scaled generated angle distribution for the original sample before selection cuts. From

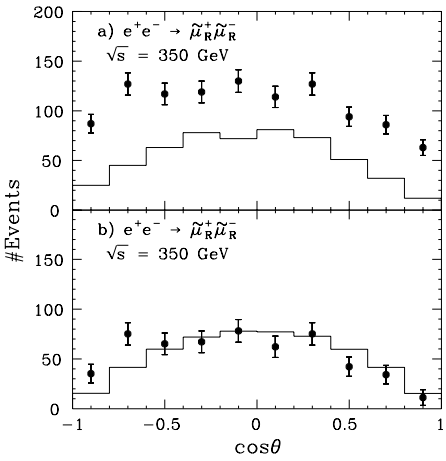

Figure 21: The production angle distribution of $\tilde{\mu}_R^-$ in $e^+e^- \to \tilde{\mu}_R^+\tilde{\mu}_R^-$ reconstructed from final-state $\mu^\pm$ momenta, knowing the $\tilde{\mu}_R^\pm$ and the $\tilde{\chi}_1^0$ masses and assuming no initial state radiation and no beamstrahlung: (a) with the two solutions unresolved and (b) with the background due to the wrong solutions subtracted. The Monte Carlo data correspond to Fig.18-c) and are plotted without acceptance corrections. The histogram in (a) is the distribution of the right solutions, while that in (b) is the distribution of the original sample before selection cuts appropriately scaled to match the number of selected events.

this, we can confirm that the angular distribution indeed behaves like $\sin^2\theta$ as expected for s-channel productions of spinless particles.

The production angle measurement is more interesting for the $\tilde{e}_R$-pair production, since the t-channel neutralino exchange diagrams may modify the angular distribution. Figs.22-a) and -b) are similar to Figs.21-a) and -b) but plotted for the $\tilde{e}_R$-pair production. We can see that the distribution has a forward peak resulting from the contribution of the t-channel diagrams. This observation alone can tell us that the lightest neutralino, which is the LSP in our case, is dominated by bino component.

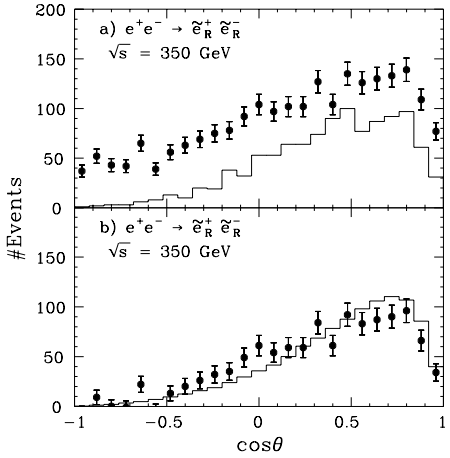

Figure 22: Similar plots to Figs.21-a) and -b) for the $\tilde{e}_R$-pair production.

4.c.2 $\tilde{\chi}_1^\pm$ Search

The LSP mass ($m_{\tilde{\chi}_1^0}$) from the slepton studies sets upper limints on the lighter chargino and the second neutralino masses through the GUT relation among the gaugino mass parameters. These upper limits are plotted in Fig.23-a) and -b) as functions of the LSP mass.

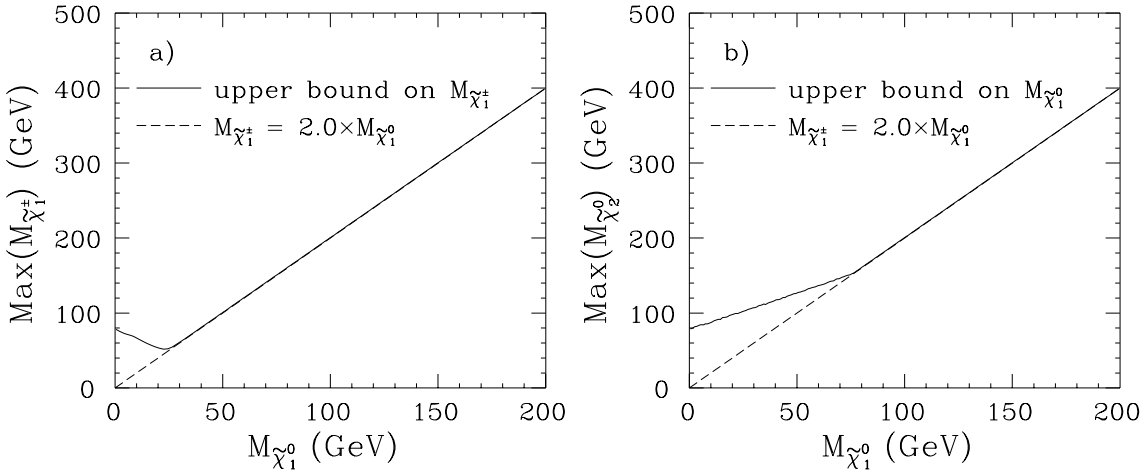

Figure 23: The upper limits on (a) the lighter chargino mass and (b) the second neutralino mass as functions of the LSP mass determined by the slepton studies.

Here, we set the center-of-mass energy just above $2 \times m_{\tilde{\chi}_1^0}$ in search of the lighter chagino pair productions. In our sample case, the lighter chargino decays directly into $\tilde{\chi}_1^0 W$ and the signature to look for is an acoplanar W pair. Fig.24 plots the acoplanarity angle between the two W candidates reconstructed from a 4-jet final state (see Ref.[15] for details of event selection). The solid line in the figure is the signal process, while the

other lines represent background processes: $e^+e^- \to W^+W^-$ (dash), $e^+e^-W^+W^-$ (dot), and the others including $\nu_e\bar{\nu}_e W^+W^-$, $e^{\pm}\overset{(-)}{\nu_e} W^{\mp}Z^0$, $W^+W^-Z^0$, etc.

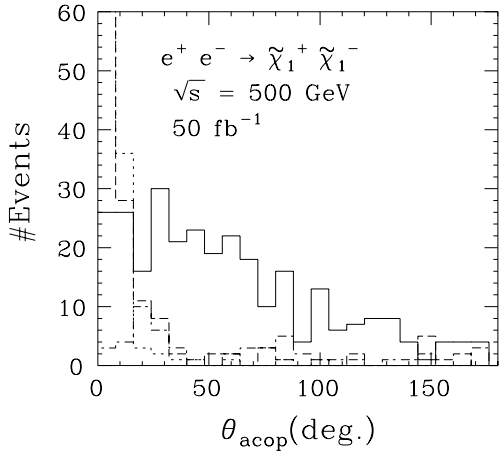

Figure 24: The acoplanarity distributions of W pairs reconstructed from 4-jet final states for the signal (solid) and the background processes: $e^+e^- \to W^+W^-$ (dash), $e^+e^-W^+W^-$ (dot), and the others including $\nu_e\bar{\nu}_e W^+W^-$, $e^{\pm}\overset{(-)}{\nu_e} W^{\mp}Z^0$, $W^+W^-Z^0$, etc.

An additional cut on the acoplanarity angle at $\theta_A = 30°$ provides a fairly clean sample of the lighter chargino pairs. As we did to the right-handed sleptons, we can determine the lighter chargino mass by measureing the end points of the W energy distribution shown in Fig.25-a). A two-parameter fit to this distribution results in the χ^2 contours in Fig.25-b). We can see that the expected error on the lighter chargino mass is $\Delta m_{\tilde{\chi}_1^{\pm}} \simeq 8$ GeV which improves to $\Delta m_{\tilde{\chi}_1^{\pm}} \simeq 5$ GeV when constrained by the LSP mass from the slepton studies.

The fact that the measured $m_{\tilde{\chi}_1^{\pm}}$ turned out to be about twice the LSP mass suggests that the lighter chargino is a wino-rich state. We can enforce this statement by measuring the production cross section for the right-handed electron beam. The charged wino, being the superpartner of the W boson, does not couple to right-handed electrons in the symmetry limit. The $\tilde{\chi}_1^{\pm}$-pair production cross section for the right-handed electron beam, thus, measures the higgsino components in the lighter chargino. Recall that the $\tilde{e}_R$-pair production cross section for the right-handed beam carries the information on the bino component in the LSP, then, by making a global fit to $m_{\tilde{\chi}_1^0}$, $m_{\tilde{\chi}_1^{\pm}}$, $\sigma_R(\tilde{e}_R^+\tilde{e}_R^-)$, and $\sigma_R(\tilde{\chi}_1^+\tilde{\chi}_1^-)$, we can determine M_1, M_2, μ, and $\tan\beta$ in principle. Notice that we did not assume the GUT relation among the gaugino mass parameters, since we want to test it here. Fig.26 shows the $\Delta\chi^2 = 1$ contour obtained from the global fit in the M_1-M_2 plane, where the dotted line represents the GUT relation. If things turn out this way, we will be forced to believe GUT.

Now that we know the chargino composition and the chargino mass, the only unknown in the cross section formula for the chargino pair production is the electron-sneutrino mass ($m_{\tilde{\nu}_e}$). Conversely, we can determine $m_{\tilde{\nu}_e}$ by measuring the chargino cross section for an unpolarized electron beam. Shown in Fig.27 are the 1-σ cross section

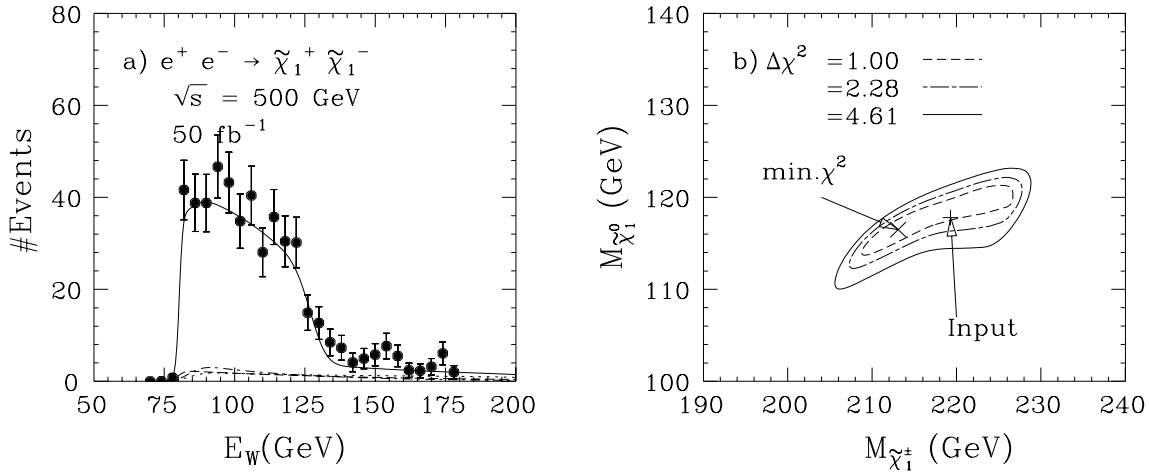

Figure 25: (a) The energy distribution of the reconstructed W candidates (points with error bars) for Monte Carlo data generated at $\sqrt{s} = 500$ GeV with an integrated luminosity of 50 fb^{-1}. The Monte Carlo events include both the signal ($e^+e^- \to \tilde{\chi}_1^+\tilde{\chi}_1^-$) and the background. The dashed, the dot-dashed, and the dotted curves show the expected background shapes for the W^+W^-, the $e^{\pm}\overset{(-)}{\nu}_e W^{\mp}Z^0$, and the other processes ($W^+W^-Z^0$, $e^+e^-W^+W^-$, $\nu_e\bar{\nu}_e W^+W^-$), respectively, while the solid line is the best-fit curve obtained from a two-parameter ($m_{\tilde{\chi}_1^0}$ and $m_{\tilde{\chi}_1^{\pm}}$) fit to the energy distribution. (b) The contours resulting from the two-parameter fit.

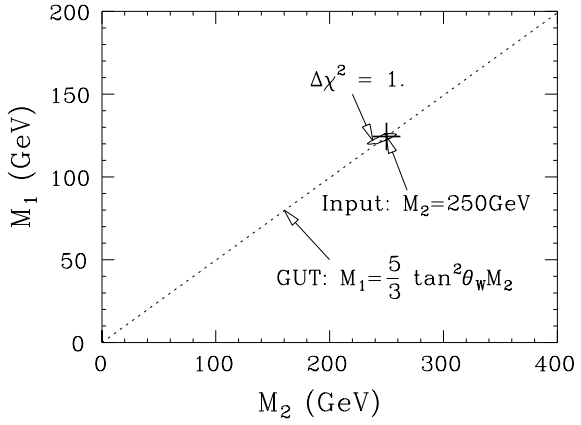

Figure 26: The $\Delta\chi^2 = 1$ contour in the M_1-M_2 plane resulting from the global fit described in the text. The dotted line is the predition of the GUT relation among the gaugino mass parameters.

bounds from the global fit (dotdash), while the dotted lines indicate the expected error from the cross section measurement.

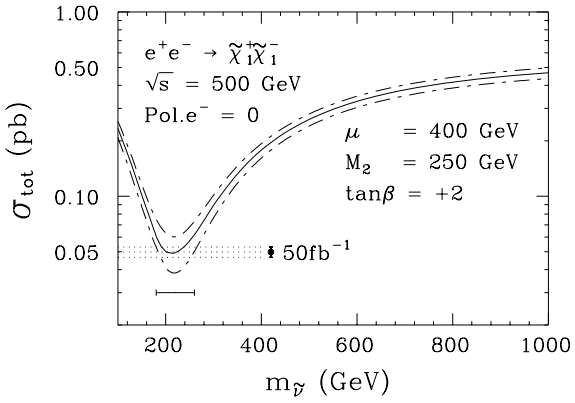

Figure 27: The 1-σ cross section bounds from the global fit (dotdash) plotted as functions of the electron-sneutrino mass. The dotted lines indicate the expected error in the cross section measurement for an integrated luminosity of 50 fb^{-1}.

In our sample case, the corresponding statistical error on the sneutrino mass is $\Delta m_{\tilde{\nu}_e} \simeq 20$ GeV. From this we can set an upper bound on the left-handed selectron mass:

$$m^2_{\tilde{e}^\pm_L} \leq m^2_{\tilde{\nu}_e} + 0.77 m^2_Z.$$

Our next target center-of-mass energt is then just above the threshold for the $\tilde{e}^+_L \tilde{e}^-_R$ pair production.

4.c.3 $\tilde{e}^\pm_L$ Search

The left-handed selectron ($\tilde{e}^\pm_L$) can be produced in the associate production process: $e^+e^-_R \to \tilde{e}^+_L \tilde{e}^-_R$, where the right-handed electron beam was chosen to suppress the standard model background. In our sample case, the direct decay ($\tilde{e}^+_L \to e^+ \tilde{\chi}^0_1$) dominates so that the signature to look for is an acoplanar e^+e^- pair. Since the right-handed electron beam removes practically all the standard model background, the remaining background comes only from $e^+e^- \to \tilde{e}^+_R \tilde{e}^-_R$. We can eliminate this background process by looking at the scatter plot of the energies of the final-state leptons. Fig.28 is such a scatter plot corresponding to the electron beam polarization of $P_{e^-} = +0.95$ and the interated luminosity of 20 fb^{-1}. We can see that the signal is well separated from the background in this scatter plot. Selecting the cluster corresponding to the signal process, we obtain a very clean sample of $\tilde{e}^+_L \tilde{e}^-_R$ associate productions.

Notice that the e^+'s carry the information on $\tilde{e}^+_L$. The positron energy distribution, thus, allows us to determine the left-handed selectron mass. Fig.29 plots the distribution of the positron energies for the selected signal sample, where the smooth curve is the best-fit curve for a two-parameter ($m_{\tilde{\chi}^0_1}$ and $m_{\tilde{e}^+_L}$) fit to the distribution. The two-parameter

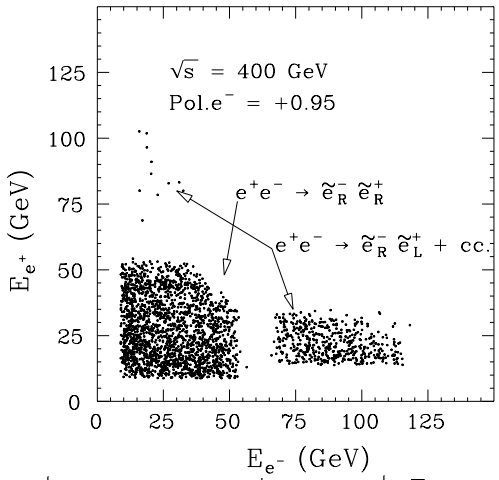

Figure 28: A scatter plot of $e^{\pm}$ energies for $e^+e^- \to \tilde{e}_L^{\pm}\tilde{e}_R^{\mp}$ and $\tilde{e}_R^{+}\tilde{e}_R^{-}$. The Monte Carlo data were generated at $\sqrt{s} = 400$ GeV with an integrated luminosity of 20 fb^{-1} and an electron beam polarization of $P_{e^-} = +0.95$, including the effects of initial state radiation and beamstrahlung.

fit resulted in the contours shown in Fig.29-b) which tells us that a 1% measurement is also possible for the left-handed selectron mass.

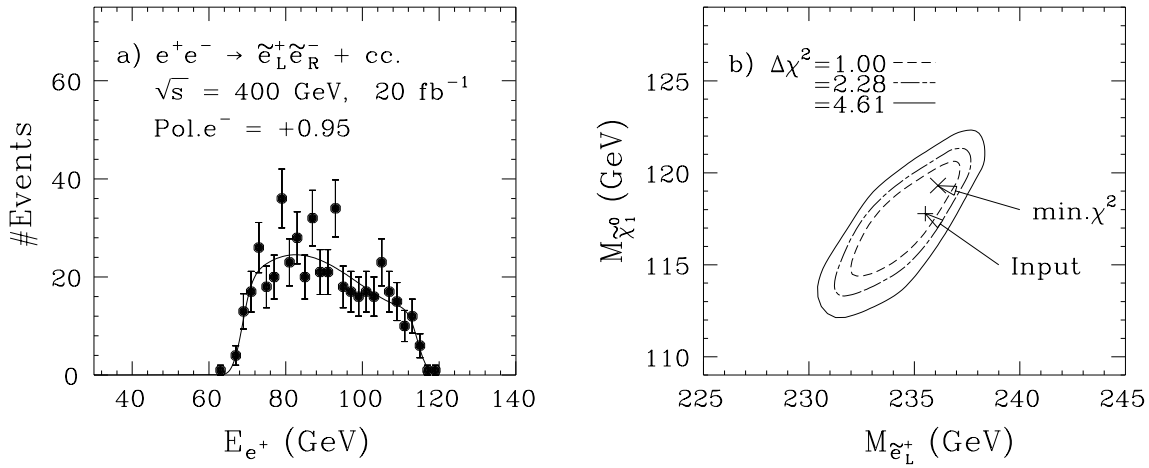

Figure 29: (a) The energy distribution of final-state positrons for the candidate $\tilde{e}_L^{\pm}\tilde{e}_R^{\mp}$ events corresponding to the signal cluster in Fig.28. The smooth line is the best-fit curve from a fit to the Monte Carlo data with the LSP and the left-handed slepton masses as free parameters. (b) The contours resulting from the two-parameter fit.

The comparison of the masses of $\tilde{e}_L$ and $\tilde{e}_R$ is of our great interest, since their squared mass difference $m^2_{\tilde{e}_L^{\pm}} - m^2_{\tilde{e}_R^{\pm}}$ relates to the squared mass difference of the $\mathbf{5}^*$ and the $\mathbf{10}$ representations of the $SU(5)$-GUT:

$$m^2_{\tilde{e}_L^{\pm}} - m^2_{\tilde{e}_R^{\pm}} = m^2_{\mathbf{5}^*} - m^2_{\mathbf{10}} + 0.53M_2^2 - 0.04m_Z^2 \cos 2\beta.$$

The last term (D-term) on the right-hand side being small, the squared mass difference of

$\tilde{e}_L$ and $\tilde{e}_R$ is essentially determined by M_2, if we assume the representation independence implied by the universal scalar mass hypothesis. Fig.30 compares the $\Delta\chi^2 = 1$ contour with the prediction of the universal scalar mass hypothesis, demonstrating that the test of the representation independence is indeed possible.

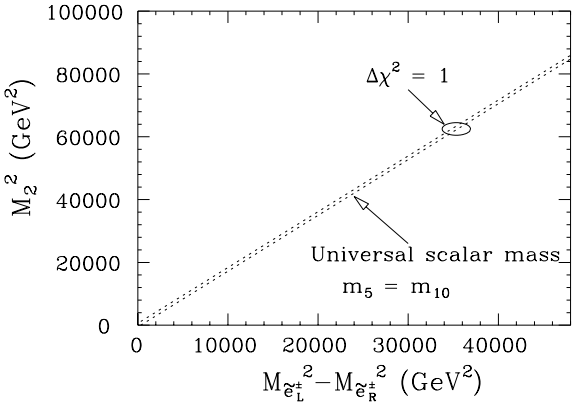

Figure 30: The $\Delta\chi^2 = 1$ contour in the plane of the squared mass difference of $\tilde{e}_L^\pm$ and $\tilde{e}_R^\pm$ and M_2^2. The dotted lines are the predictions of the universal scalar mass hypothsis for $\tan\beta = 0$ and 30.

4.d If There is No Light Higgs

Up to this point, we have been assuming the existence of a light Higgs boson. As stressed earlier, if there is no light Higgs boson found at next-generation linear e^+e^- colliders, that implies the death of low energy supersymmetry and GUT, and will make a very strong impact on high energy physics. In this case, we need to learn as much as possible from what we have at hand: W, Z, and top. Here, let us briefly discuss what we can do in the absence of light Higgs bosons.

4.d.1 Higgs Search in Loops

In the standard model, the Higgs mass, the W mass, and the top mass are interrelated through radiative corrections, which is very powerful as demonstrated by top mass predictions using recent LEP data. Considering the precision on the top and the W masses expected at future linear e^+e^- colliders, we may hope to measure the Higgs mass through the loop effects. Fig.31 shows the effect of the precision top mass measurement on the indirect Higgs mass measurement. We can see that the 1-σ contour quickly shrinks down with the improvement of the top mass measurement.

Fig.32 plots the 1-σ Higgs mass bounds as functions of the Higgs mass, when $\Delta m_W = 21$ MeV and $\Delta m_t = 0.5$ GeV.

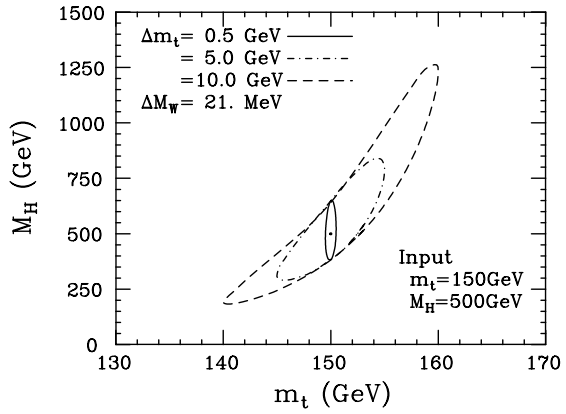

Figure 31: The 1-σ contours in the m_t-m_H plane for $\Delta m_W = 21$ MeV and $\Delta m_t = 0.5$ (solid), 5.0 (dotdash), and 10.0 (dash)GeV. The input values are $m_t = 150$ GeV and $m_H = 500$ GeV.

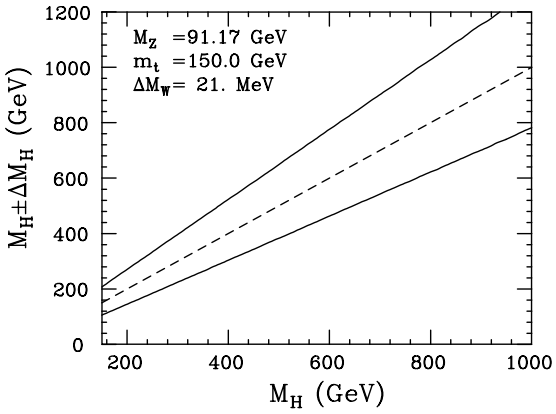

Figure 32: The 1-σ bounds on the Higgs mass as a function of the input Higgs mass when we assume $\Delta m_W = 21$ MeV and $\Delta m_t = 0.5$ GeV.

4.d.2 Self-Couplings of W, Z, and γ

If the Higgs mass estimated indirectly from the loop effects turns out to be very heavy, the most likely scenarios are those based on a strongly interacting Higgs sector. Then one of the most crucial questions is whether only the longitudinal components of W and Z are composite or both of their transverse and longitudinal components are composite. In the latter case, there must be some anomalous self-couplings among W, Z, and γ. A linear e^+e^- collider is an ideal machine to detect such anomalous self-couplings[16, 17].

Fig.33 shows the expected limits on the anomalous couplings, $\Delta\kappa_\gamma$ and λ, from various reaction channels availabe at future linear e^+e^- colliders[17]. The anomalous couplings are related to the electrostatic properties of the W boson through

$$\mu_W = \frac{e}{2m_W}(2 + \Delta\kappa_\gamma + \lambda)$$

$$Q_W = \frac{e}{m_W^2}(-1 - \Delta\kappa_\gamma + \lambda)$$

and are expected to be zero at the tree level calculations in the standard model. We can see that there are a lot of independent processes to test the compositeness and the expected errors on the anomalous self-couplings reach one percent level.

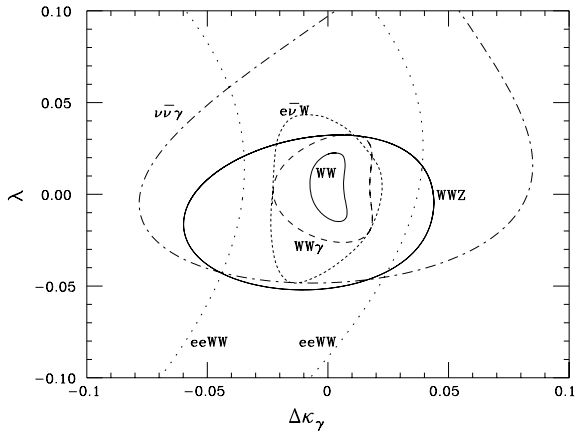

Figure 33: The expected 95% cofidence level limits on the anomalous self-couplings, $\Delta\kappa_\gamma$ and λ, from various processes avaialbe at a future linear e^+e^- collider with $\sqrt{s} = 500$ GeV and $\int Ldt = 50$ fb^{-1}.

Fig.34 compares the one-parameter sensitivity to anomalous self-couplings expected at various machines. Notice that linear colliders are indispensable to push down the limits on $\Delta\kappa_\gamma$ and $\Delta\kappa_Z$.

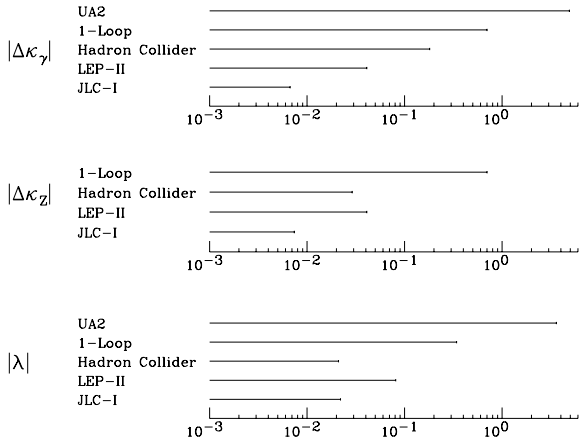

Figure 34: Comparison of various machines in terms of the one-parameter precisions on the anomalous self-couplings, $\Delta\kappa_\gamma$, $\Delta\kappa_Z$, and λ. In the figure, 1-Loop means the indirect limits from low energy data. See Ref.[17] for details.

5 Summary and Conclusion

There are strong motivations for construction of a linear e^+e^- collider in the energy range $\sqrt{s} = 300 \sim 500$ GeV, including (i) the top quark is there, and (ii) a light Higgs is likely as suggested by the measured $\sin^2\theta_W$ being consistent with the SUSY-$SU(5)$-GUT prediction. The existence or non-existence of a light Higgs boson is one of the most important branch points to decide the future direction of high energy physics. The linear e^+e^- collider is a sure-fire machine to answer this crucial question.

The accelerator technology for constructin of such a machine has almost matured: almost all of the previously conceived technological problems have been solved at least in principle. We will be ready for construction in three years.

There are rich physics which allow a consistent and systematic physics program ranging from discoveries to precision studies. The following are only a few of what we could cover today.

At the $t\bar{t}$ threshold, we can determine the top mass to $\Delta m_t \simeq 0.2$ GeV, given an integrated luminosity of 10 fb^{-1}. Accumulating more statistics at some optimal energy in the threshold region, we can carry out precision measurements of $\alpha_s(m_Z)$ and Γ_t: $\Delta\alpha_s(m_Z) \simeq 0.002$ and $\Delta\Gamma_t/\Gamma_t \simeq 0.04$ for an integrated luminosity of 100 fb^{-1}.

If the Higgs boson is kinematically accecible, we can measure its mass and width with $\Delta m_H \simeq$ 10-50 MeV and $\Delta\Gamma_H \simeq 200$ MeV for an integrated luminosity of 10 fb^{-1}. Precision studies of the Higgs properties will then allow us to judge whether the discovered Higgs boson is that of the standard model or not.

If there is such a light Higgs, SUSY is likely to come next. Discoveries of SUSY particles are easy at a linear e^+e^- collider, once its energy crosses their production thresholds. Once a SUSY particle is found, we can study its properties in detail, and learn a lot about the SUSY parameters. The information on the SUSY parameters allows us to predict the mass of the next SUSY particle, and guides us to its discovery. Moreover, the measurements of the SUSY parameters will enable us to get insight into the structure of the SUSY breaking sector and will open up a window to Planck scale physics.

Even if there is no light Higgs to be found at the next-generation linear e^+e^- collider, the machine will provide very important information to decide which way to go.

In conclusion, a linear e^+e^- collider covering $\sqrt{s} = 300 \sim 500$ GeV is well motivated and technologically feasible and can be more than complementary to hadron colliders from physics point of view.

References

[1] P. Langacker, talk given at this symposium, in these proceedings.

[2] Y. Okada, M. Yamaguchi, and T. Yanagida, *Prog. Theor. Phys.* **85** (1991) 1, *Phys. Lett.* **B62** (1991) 54; J. Ellis, G. Ridolfi, and F. Zwirner, *Phys. Lett.* **B257** (1991) 83; H. Haber and R. Hempfling, *Phys. Rev. Lett.* **66** (1991) 1815.

[3] T. Moroi and Y. Okada, *Tohoku preprint* TU-405 (1992).

[4] *Proceedings of the 5th International Workshop on Next-Generation Linear Colliders*, SLAC-436 (1993).

[5] H. Matsumoto, private communication; see also S. Takeda, M. Akemoto, J. Urakawa, K. Oide, T. Naito, H. Hayano, and H. Matsumoto, KEK Proceedings 93-10 (1993) 53.

[6] J. Urakawa, *Proceedings of the 4th Workshop on JLC*, KEK Proceedings 94-1 (1994) 64.

[7] *FFTB Project Design Report*, SLAC-Report-376 (1991).

[8] JLC Group, KEK Report 92-16 (1992).

[9] V. Fadin and V. Khoze, *Sov. J. Nucl. Phys.* **48** (1988) 309; M. Strassler and M. Peskin, *Phys. Rev.* **D43** (1991) 1500.

[10] S. Komamiya, *Proceedings of the 1990 Summer Study on High Energy Physics*, 1990, Snowmass, edited by E. Berger, World Scientific p459, also available as SLAC-PUB-5324 (1991); K. Fujii, *Proceedings of Workshop on Physics and Experiments with Linear Colliders*, Saariselkä, Finland, September 1991, edited by R. Orava, P. Eerola, and M. Nordberg, World Scientific, p203, also available as KEK Preprint 92-6 (1992); R. Miquel, talk given at *Workshop on Physics and Experiments with Linear Colliders*, Saariselkä, Finland, September 1991; see also DESY 92-123A (1992) 327.

[11] Y. Sumino, K. Fujii, K. Hagiwara, H. Murayama, and C. Ng, *Phys. Rev.* **D47** (1993) 56; M. Jeżabek, J. Kühn, and T. Teubner, *Z. Phys.* **C56** (1992) 653.

[12] K. Fujii, T. Matsui, and Y. Sumino, KEK Preprint 93-125 (1993).

[13] K. Kawagoe and S. Orito, UT-ICEPP 92-06 (1992); S. Janot, *Proceedings of Workshop on Physics and Experiments with Linear Colliders*, Waikoloa, Hawaii, April 1993, edited by F.A. Harris, S.L. Olsen, S. Pakvasa, and X. Tata, World Scientific, p192.

[14] J. Grivaz, *Proceedings of Workshop on Physics and Experiments with Linear Colliders*, Saariselkä, Finland, September 1991, edited by R. Orava, P. Eerola, and M. Nordberg, World Scientific, p353.

[15] T. Tsukamoto, K. Fujii, H. Murayama, M. Yamaguchi, and Y. Okada, KEK Preprint 93-146 (1993).

[16] T. Barklow, *Proceedings of Workshop on Physics and Experiments with Linear Colliders*, Saariselkä, Finland, September 1991, edited by R. Orava, P. Eerola, and M. Nordberg, World Scientific, p423.

[17] A. Miyamoto, *Proceedings of Workshop on Physics and Experiments with Linear Colliders*, Waikoloa, Hawaii, April 1993, edited by F.A. Harris, S.L. Olsen, S. Pakvasa, and X. Tata, World Scientific, p141.